Astronomy & Astrophysics manuscript no. output
July 13, 2026

High $^{12}C/^{13}C$ isotopic ratios toward G+0.693-0.027: Evidence for gas inflow to the Central Molecular Zone

L. Colzi[1], O. Sipilä[2], I. Jiménez-Serra[1], V. M. Rivilla[1], M. Sanz-Novo[2], S. Martín[3,4], and S. Zeng[5]

[1] Centro de Astrobiología (CAB), CSIC-INTA, Ctra. de Ajalvir Km. 4, 28850, Torrejón de Ardoz, Madrid, Spain
e-mail: lcolzi@cab.inta-csic.es
[2] Max-Planck-Institut für Extraterrestrische Physik (MPE), Giessenbachstr. 1, 85748 Garching, Germany
[3] European Southern Observatory, Alonso de Córdova 3107, Vitacura 763 0355, Santiago, Chile
[4] Joint ALMA Observatory, Alonso de Córdova 3107, Vitacura 763 0355, Santiago, Chile
[5] Star and Planet Formation Laboratory, Cluster for Pioneering Research, RIKEN, 2-1 Hirosawa, Wako, Saitama, 351-0198, Japan

Received 30 April 2026; Accepted 07 July 2026

ABSTRACT

Context. Isotopic ratios are essential tools for understanding Galactic chemical evolution and reconstructing the star formation history of the Milky Way, as different isotopes are produced through distinct stellar nucleosynthesis processes. While the $^{12}C/^{13}C$ ratio is known to increase with galactocentric distance in the Galactic disk, measurements in the Central Molecular Zone (CMZ), which are often made more difficult by high line optical depth effects, have historically yielded low values (~3–30).
Aims. The aim of this work is to determine the initial $^{12}C/^{13}C$ isotopic ratio for the parent material of the CMZ molecular cloud G+0.693−0.027. By employing optically thin molecular tracers and applying corrections for isotopic fractionation effects, we provide a more accurate constraint on the nucleosynthetic enrichment history of the Galactic center.
Methods. We used an ultrahigh-sensitivity spectral survey carried out with the IRAM 30m and Yebes 40m telescopes to detect single and double ^{13}C-isotopologues of HC_3N and HC_5N. We analyzed the data and derived the column densities and isotopic ratios, which were then compared with astrochemical models including ^{13}C- and ^{15}N-isotopologues to account for potential degree of isotopic fractionation.
Results. We derived $^{12}C/^{13}C$ ratios of 36.7±1.02 for the main velocity component of HC_3N (from double isotopologues) and 38.8±1.5 for HC_5N. These values are significantly higher than typical CMZ measurements from simpler species. Our models suggest low to intermediate fractionation degrees at early timescales ($<3\times10^4$ yr), leading to an inferred initial $^{12}C/^{13}C$ ratio of ~48 for the material from which the present-day CMZ molecular clouds formed.
Conclusions. The derived ratios (37–48) are consistent with those found at galactocentric distances of 3–5 kpc. This supports a scenario where the CMZ is replenished by gas inflows from the Galactic disk, likely driven by the Galactic bar, with a possible contribution from the accretion of less-processed material from external sources such as dwarf galaxies.

Key words. Astrochemistry – Line: profiles – ISM: molecules – Galaxy: center – Galaxy: evolution – Radio lines: ISM

1. Introduction

Understanding the chemical evolution driven by stellar nucleosynthesis is essential in order to reconstruct the star formation history of galaxies (e.g., Maiolino & Mannucci 2019; Arcones & Thielemann 2023). Galactic chemical evolution (GCE) models are widely employed to constrain stellar nucleosynthesis processes and the formation timescales of the different Galactic components (halo, bulge, and thick and thin disks; e.g., Matteucci 2021). They also provide valuable insights into the initial mass function of external galaxies (e.g., Romano et al. 2017; Zhang et al. 2018).

In the Milky Way, GCE models adopting different nucleosynthesis prescriptions predict trends that are broadly consistent with the elemental abundances measured in stellar atmospheres as a function of metallicity for stars in the solar neighborhood. However, the abundances of the less common isotopes (such as ^{13}C, ^{15}N, ^{18}O, and ^{34}S) are more difficult to determine in stars as their spectral features are weaker than those of the main isotopes. These isotopic ratios can generally be measured only in highly evolved giant stars where strong spectral features are detectable, but the original isotopic composition has already been altered and is not pristine any longer (e.g., Tautvaišienė et al. 2016). Measurements of $^{12}C/^{13}C$ and $^{16}O/^{18}O$ ratios in unevolved stars are scarce; only a few studies are available (e.g., Botelho et al. 2020). Therefore, to overcome this limitation, isotopic ratios measured toward Galactic molecular clouds are commonly employed to constrain the GCE as a function of the galactocentric distance (R_{GC}; see, e.g., Wilson & Matteucci 1992; Wilson & Rood 1994; Milam et al. 2005; Colzi et al. 2018; Yan et al. 2019; Jacob et al. 2020; Kobayashi et al. 2020; Colzi et al. 2022b; Böhm et al. 2026).

For this work we focused on the carbon isotopic ratio, $^{12}C/^{13}C$. ^{12}C is a primary element, formed directly from H and He during He-burning in the interiors of red giants and supergiants (e.g., Burbidge et al. 1957; Woosley et al. 2002; Karakas & Lattanzio 2014). Conversely, ^{13}C has a distinct origin, with a primary production channel in massive low-metallicity rotating stars (e.g., Chiappini et al. 2008; Prantzos et al. 2018), and a secondary production pathway requiring pre-existing ^{12}C and ^{16}O seeds through the cold and hot CNO cycles operating in main-sequence stars and nova explosions, respectively (Romano

Article published by EDP Sciences, to be cited as https://doi.org/10.1051/0004-6361/202660705

2022). Observational studies of various molecular species (e.g., CN, CH, CS, CO, and H_2CO) toward molecular clouds located at different galactocentric distances (R_{GC}) have revealed an increasing trend of $^{12}C/^{13}C$ with R_{GC}, ranging from ∼30 at 2 kpc to ∼80 at 11 kpc (e.g., Milam et al. 2005; Yan et al. 2019; Jacob et al. 2020; Yan et al. 2023). These observations have been compared with GCE models by Romano et al. (2017, 2019) and Colzi et al. (2022b), which constrained stellar nucleosynthesis prescriptions in the range R_{GC} = 4–11 kpc. Their models successfully reproduce the observed linear increase in $^{12}C/^{13}C$ with R_{GC}.

In the Central Molecular Zone (CMZ; the inner ∼300 pc of our Galaxy), the $^{12}C/^{13}C$ ratio has been extensively measured over the past five decades with the advent of radio astronomical observations. Measurements toward molecular clouds such as Sgr B2 and Sgr A, obtained from both absorption and emission lines, have yielded values ranging from ∼3 to 30 for simple molecules including HC_3N, H_2CO, OCS, HCO^+, HCN, HNC, C_3, and CH (Fomalont & Weliachew 1973; Wannier & Linke 1978; Gardner & Whiteoak 1979; Goldsmith & Linke 1981; Gardner & Whiteoak 1982; Guesten et al. 1985; Turner 1991; Riquelme et al. 2010; Giesen et al. 2020b; Jacob et al. 2020). Furthermore, values of ∼20–32 have been derived from complex organic molecules (COMs), carbon-bearing species with six or more atoms (Herbst & van Dishoeck 2009), such as methanol (CH_3OH), methyl cyanide (CH_3CN), ethanol (CH_3CH_2OH), vinyl cyanide (C_2H_3CN), and ethyl cyanide (C_2H_5CN) (e.g., Müller et al. 2008; Belloche et al. 2013, 2016; Müller et al. 2016; Margulès et al. 2016; Halfen et al. 2017).

These values are broadly consistent with the increase in the $^{12}C/^{13}C$ ratio with R_{GC} and with an extrapolation of the observed Galactic trend toward the CMZ, yielding values of ∼10–20. From the perspective of stellar nucleosynthesis, this behavior is expected: the higher metallicity in the CMZ could lead to a higher relative production of ^{13}C with respect to ^{12}C. In this scenario, ^{12}C is primarily produced by first-generation massive stars on short timescales, whereas ^{13}C is mainly synthesized through CNO processing of ^{12}C in lower-mass stars over longer evolutionary timescales (e.g., Prantzos et al. 1996). However, Wilson & Rood (1994) already pointed out that the chemical evolution of the Galactic disk and that of the Galactic center may differ, and there is no basis for assuming that the abundance or isotopic gradients observed in the disk continue smoothly into the central regions. From an observational point of view, most of the reported $^{12}C/^{13}C$ values have been derived using the direct method, that is, by comparing the line intensities of the main isotopolog (e.g., HCO^+ or HCN) with those of its counterpart with ^{13}C (e.g., $H^{13}CO^+$ or $H^{13}CN$). However, these measurements are strongly affected by line optical depth effects, and thus generally represent lower limits. It is worth noting that values derived from COMs tend to lie within the upper range of those obtained from simpler species, as COM transitions are typically optically thinner. Moreover, more robust estimates, relying on optically thin tracers and double-isotopolog techniques, have also been obtained in the literature. In particular, Humire et al. (2020) and Yan et al. (2023) determined the carbon isotopic ratio using the $C^{34}S/^{13}C^{34}S$ pair toward the +50 km s^{-1} cloud and along the Sgr B2 line of sight, respectively, finding values in the range 22–35.

Finally, isotopic fractionation processes in gas-phase chemistry may also contribute to lowering the $^{12}C/^{13}C$ in molecular species and should therefore be taken into account (e.g., Colzi et al. 2020). Isotopic fractionation refers to the enrichment or depletion of specific isotopes–such as ^{13}C relative to ^{12}C–within molecules due to small differences in reaction rates during isotopic exchange reactions. These effects arise from differences in zero-point energy (ZPE) between isotopologues, leading to temperature-dependent fractionation in which the heavier isotope is preferentially incorporated into the more stable molecular form (e.g., Caselli & Ceccarelli 2012; Roueff et al. 2015).

Table 1: Properties of the two velocity components toward G+0.693 studied in this work, as found by Colzi et al. (2024).

Component	RA(ICRS) (h m s)	Dec(ICRS) (° ′ ″)	n_{H_2} (cm^{-3})	T_{kin} (K)
C1[a]	17:47:22.00	-28:21:27.00	2×10^4	140
C2	17:47:21.83	-28:21:20.57	5×10^4	30

Notes. [(a)] The observations described in this paper are centered on these coordinates.

Several recent studies have indicated that the metallicity gradient in the inner Milky Way may flatten toward the Galactic center (e.g., Ryde & Schultheis 2015; Kovtyukh et al. 2019; Feldmeier-Krause et al. 2020; Chen et al. 2023; Matsunaga et al. 2023). In view of this, investigations of isotopic ratios, such as $^{12}C/^{13}C$, in molecular gas within the CMZ become especially timely, since isotopic signatures offer a complementary probe of the Galactic chemical evolution under different metallicity conditions and different timescales (e.g., Grieco et al. 2015; Romano et al. 2017). In our work, we aim to determine the initial $^{12}C/^{13}C$ ratio of the material from which G+0.693 formed, which reflects the stellar nucleosynthetic enrichment history of the CMZ. To this end, we used observations of single and double isotopologues of HC_3N and HC_5N toward the G+0.693−0.027 molecular cloud (hereafter G+0.693), identifying those species with negligible line opacity, and combined the derived isotopic ratios with astrochemical models to determine the degree of isotopic fractionation.

This work is the first paper in a series aimed at building a comprehensive inventory of isotopic ratios in the CMZ source G+0.693. These studies will provide a direct link with isotopic ratio measurements in extragalactic sources, which are now becoming accessible, for example through the recent ALMA large observational programs the ALMA Comprehensive High-resolution Extragalactic Molecular Inventory (ALCHEMI) toward the nearby starburst galaxy NGC 253 (e.g. Martín et al. 2021; Butterworth et al. 2024). The paper is organized as follows. In Sect. 2 we describe the target source and the observational data used in this study. The analysis procedures and the main observational results are presented in Sect. 3.1. The fractionation degree is then investigated using astrochemical models in Sect. 3.2. The implications of the main results are discussed in Sect. 4, and our conclusions are summarized in Sect. 5.

2. Source and observations

In this section, we describe the main physical and astrochemical properties of the G+0.693 molecular cloud and summarize the observational datasets employed in this study.

2.1. The G+0.693–0.027 CMZ molecular cloud

G+0.693 is located in the Sgr B2 region. This cloud is found to be extremely prolific from an astrochemical point of view, as many molecules–including numerous COMs–have been detected, some of them for the first time (Zeng et al. 2018; Rivilla et al. 2019; Jiménez-Serra et al. 2020; Rivilla et al.

2021; Rivilla et al. 2023; Rodríguez-Almeida et al. 2021b; Jiménez-Serra et al. 2022; Sanz-Novo et al. 2023; Zeng et al. 2023; San Andrés et al. 2024; Sanz-Novo et al. 2025; Araki et al. 2026).

G+0.693 lies approximately 55″ northeast of Sgr B2(N), a region well known for its intense ongoing star formation (e.g., Schmiedeke et al. 2016; Ginsburg et al. 2018). In contrast, G+0.693 shows no signposts of current high-mass star formation activity, such as UC HII regions, H_2O or Class II methanol masers, or strong dust continuum sources (e.g., Ginsburg et al. 2018; Zeng et al. 2020). Zeng et al. (2020) proposed that G+0.693 is currently affected by a cloud–cloud collision, producing the shocks responsible for its rich chemistry (e.g., Requena-Torres et al. 2006; Martín et al. 2008; Armijos-Abendaño et al. 2020). Recent observations toward G+0.693 reveal a broad line component associated with an extended, warm, and diffuse molecular gas structure (C1), as well as two denser and colder condensations (C2 and C3) embedded within it. These condensations appear to be in a post-shock evolutionary stage and are characterized by enhanced deuteration (high D/H ratios) (Colzi et al. 2022a, 2024). These results suggest that G+0.693 may represent the prestellar precursor of a future massive star-forming cluster within the Sgr B2 complex. Altogether, these results highlight G+0.693 as a unique laboratory for investigating the interplay between shocks, potential sites of future star formation, and molecular complexity in the CMZ.

In this work, we focus on the study of carbon isotopic ratios for the C1 and C2 line components analyzed by Colzi et al. (2024). The coordinates and physical properties for these two gas components are listed in Table 1.

2.2. Observations

The work presented here makes use of an ultrahigh-sensitivity spectral survey toward the G+0.693 molecular cloud, carried out with the IRAM[1] 30m (Granada, Spain) and Yebes 40m (Guadalajara, Spain) radio telescopes. These datasets have been previously used in several studies (e.g., Rivilla et al. 2021; Colzi et al. 2022a; Jiménez-Serra et al. 2022; Rivilla et al. 2022; Sanz-Novo et al. 2023; Colzi et al. 2024). The observations were performed in position-switching mode, centered at α_{ICRS} = $17^h47^m22^s$ and δ_{ICRS} = −28°21′27″, with an off position offset by (−885″, +290″). The spectral line intensities are expressed in terms of the antenna temperature, T_A^*, corrected for atmospheric attenuation, radiative losses, and rearward scattering and spillover. This approximation is appropriate given the extended molecular emission observed toward G+0.693, which extends well beyond the primary beams of the telescopes (e.g., Brünken et al. 2010; Jones et al. 2012; Li et al. 2020; Zheng et al. 2024).

The IRAM 30m and Yebes 40m observations used in this work were obtained from ultra-deep spectral surveys reaching sub-mK noise levels. The IRAM 30m data combine observations from projects 172–18 (PI: Martín-Pintado; April 2019), 018–19 and 133–19 (PI: Rivilla; August and December 2019), and 123–22 (PI: Jiménez-Serra; February 2023). These cover the frequency ranges 71.76–116.72 GHz, 124.77–175.5 GHz, 199.8–238.29 GHz, 252.52–260.30 GHz, and 268.2–275.98 GHz. The spectra were smoothed to 615 kHz, corresponding to a velocity resolution of 1.0–2.2 km s^{-1}, adequate to resolve the typical line widths of 15–20 km s^{-1} observed in the region (e.g., Rivilla et al. 2020; Rivilla et al. 2021; Colzi et al. 2022a, 2024). The achieved root mean square (rms) noise levels are 1.7–2.8 mK (71–90 GHz), 1.5–9.8 mK (90–115 GHz), 3.1–6.8 mK (124–175 GHz), 4.7–9.7 mK (200–238 GHz), and 10.8–18 mK (250–275 GHz). The beam varies from 10″ up to 32″ within the frequencies covered.

The Yebes 40m observations were obtained between March 2021 and March 2022 (project 21A014; PI: Rivilla), covering the 31.07–50.42 GHz range, with a total on-source time of 110 hr.[2] The final spectra were smoothed to 256 kHz (velocity resolution of 1.5–2.5 km s^{-1}), yielding rms noise levels of 0.25–0.9 mK across the band. The beam varies from 36.4″ up to 54.4″ within the frequencies covered.

3. Analysis and results

3.1. Observational results

To reliably derive the $^{12}C/^{13}C$ isotopic ratio of HC_3N and HC_5N, we searched for all possible single- and double-^{13}C isotopologues of these species. Figures 1–3 and A.1–A.6 show the rotational transitions of $H^{13}CCCN$, $HC^{13}C^{13}CN$, $HC_4^{13}CN$, $HC^{13}CCN$, $HCC^{13}CN$, $H^{13}C^{13}CCN$, $H^{13}CC^{13}CN$, $H^{13}CC_4N$, $HC^{13}CC_3N$, $HC_3^{13}CCN$, and $HC_2^{13}CC_2N$ detected toward G+0.693. In addition, Appendix B presents the HC_5N transitions covered in our data. Their spectroscopic information is taken from the Cologne Database for Molecular Spectroscopy[3] (CDMS; Müller et al. 2001, 2005; Endres et al. 2016). The entries of the catalog for these species are based on the laboratory works of de Zafra (1971); Alexander et al. (1976); Creswell et al. (1977); Mallinson & de Zafra (1978); Winnewisser et al. (1982); Chen et al. (1991); Yamada et al. (1995); Thorwirth et al. (2000, 2001); Bizzocchi et al. (2004); Giesen et al. (2020a); Sanz et al. (2005). The dipole moments were determined by Alexander et al. (1976); DeLeon & Muenter (1985). We note that we do not display and use in the analysis the rotational transitions that are heavily blended with other molecular species or whose emission lies below the noise level. Only in a few cases–such as $H^{13}C^{13}CCN$, discussed below–these transitions are shown since they provide further support for the derived model fits. In fact, some transitions are blended with lines from other species, but their predicted intensities remain useful for reproducing the observed spectra once the contributions of all species previously identified toward G+0.693 are included. Furthermore, the hyperfine structure (HFS) of the molecular transitions is neglected in our line profile modeling. In our observations, the maximum frequency separation due to HFS occurs in the $HC_3N(J = 5 - 4)$ transition, where the $F = 4 \rightarrow 3$ component is offset from the $F = 6 \rightarrow 5$ component by 0.2494 MHz. This corresponds to a velocity separation of $\approx$ 1.6 km s^{-1}, which is negligible given the broad observed line widths (FWHM $\approx$ 20 km s^{-1}). Since HFS splitting scales inversely with the rotational quantum number J, these components remain unresolved and do not significantly contribute to the observed line profiles.

To derive the total column densities of all molecules, we performed a local thermodynamic equilibrium (LTE) analysis. For HC_5N, we carried out a dedicated analysis following the same methodology applied to HC_3N in Colzi et al. (2024). The full set of observed transitions cannot be simultaneously reproduced under LTE conditions. In fact, possible non-LTE effects introduce a curvature in the rotational diagram (Goldsmith & Langer

[1] Institut de Radioastronomie Millimétrique.

[2] Individual observing sessions were performed between 2021 March and 2022 March; see Rivilla et al. (2023) and Sanz-Novo et al. (2023) for details.

[3] http://cdms.astro.uni-koeln.de/classic/

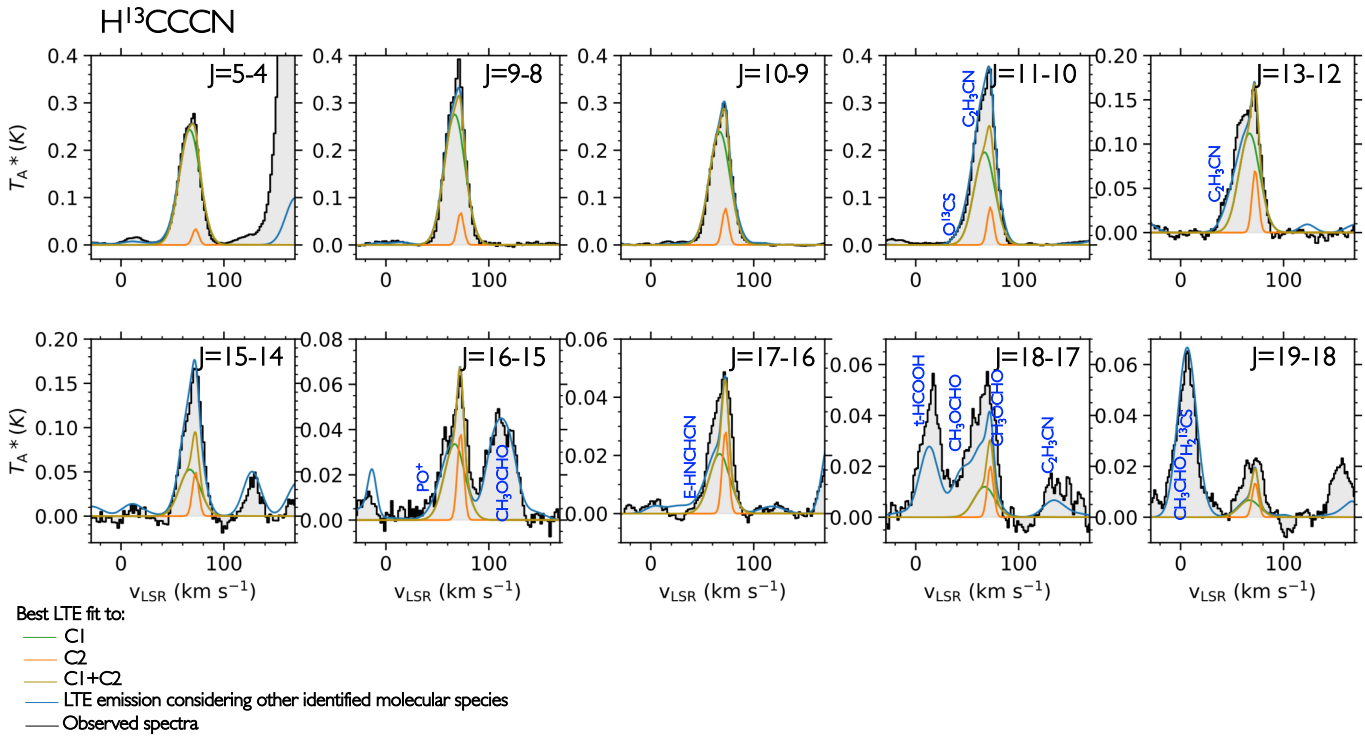

Fig. 1: $H^{13}CCCN$ observed transitions used for the LTE analysis (black histogram). For each panel, the corresponding transition is indicated in the upper right corner. The green and orange solid lines are the best LTE fit to the C1 and C2 components, respectively. The dark gold line is the sum of the two components. The blue line indicates the total modeled line emission, including the contribution of all molecular species previously identified in the survey.

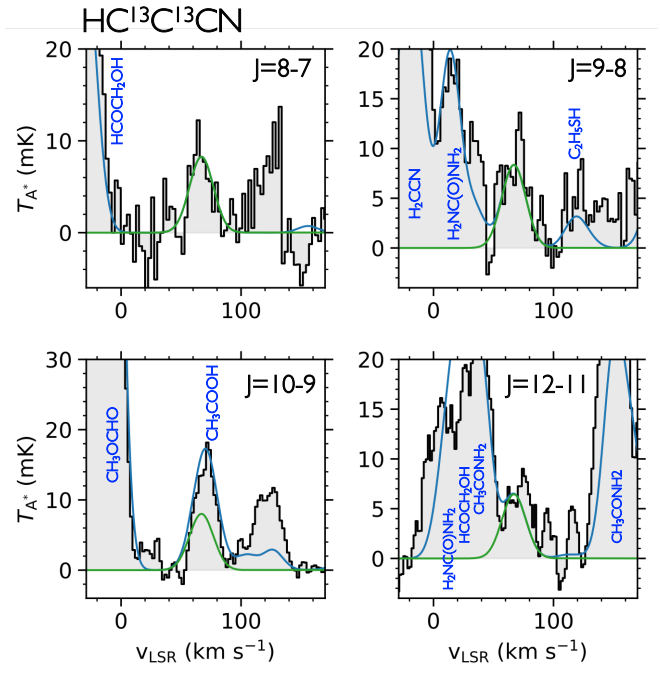

Fig. 2: Same as Fig. 1 but for $HC^{13}C^{13}CN$. In this case only the C1 component modeled in green is detected, as explained in Sect. 3.1.

1999), as illustrated in Fig. 2 of Colzi et al. (2024). Thus, as in the previous work, we first excluded all transitions with upper-level energies E_{up} < 5 K (J = 5–4 and 7–6), whose observed intensities exceed the predictions of LTE models. These two low-energy transitions of HC_5N are therefore not considered further in the analysis. The remaining transitions were separated into two groups: (i) 5 < E_{up} ≤ 70 K (low-J, from J = 12–11 to 32–31; Fig. B.1), and (ii) E_{up} > 70 K (high-J, from J = 33–32 to 43–42; Fig. B.2). Transitions at even higher J are too faint to be detected in our data. We note that for HC_3N and its isotopologues the low-J regime is defined for 5 < E_{up} ≤ 100 K (see also Colzi et al. 2024). For HC_5N we have redefined this in order to cover the same energy range as its ^{13}C-isotopologues, for which only transitions with E_{up} < 70 K have been detected. We verified that extending the HC_5N analysis up to E_{up}=100 K (i.e., including transitions up to J=39–38) does not significantly affect the derived total column density, yielding consistent values within the uncertainties ((1.248±0.011)×10^{14} cm^{-2} and (1.247±0.018)×10^{14} cm^{-2}).

For the ^{13}C isotopologues of HC_3N and HC_5N studied here, only transitions corresponding to the low-J regime of the main isotopologues are detected, as the high-J lines remain below the noise level. Thus, all isotopic ratios discussed in the following are derived exclusively from these low-J transitions. Finally, we note that the C1 velocity component is detected in all species analyzed, whereas the C2 component is detected only for the main isotopologues HC_3N and HC_5N, and for the single ^{13}C-isotopologues of HC_3N.

To fit the groups of transitions under LTE conditions, we used the Spectral Line Identification and Modeling (SLIM) tool (version from 2024, June 15) within the MADCUBA software package, which generates synthetic spectra assuming LTE and taking line opacity into account. For each transition, SLIM computes the convolution of a Gaussian source distribution with the corresponding Gaussian telescope beam; further details are provided in Sect. 3.2.2 of Martín et al. (2019a). The physical parameters

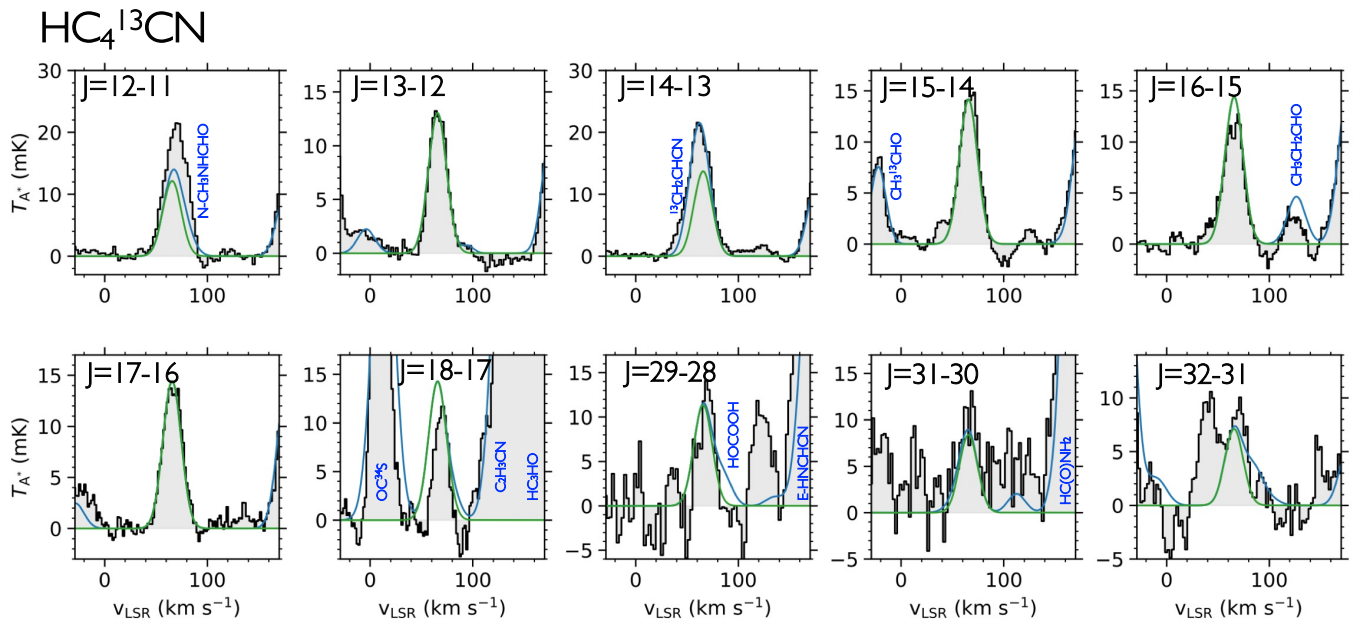

Fig. 3: Same as Fig. 2 but for $HC_4{}^{13}CN$.

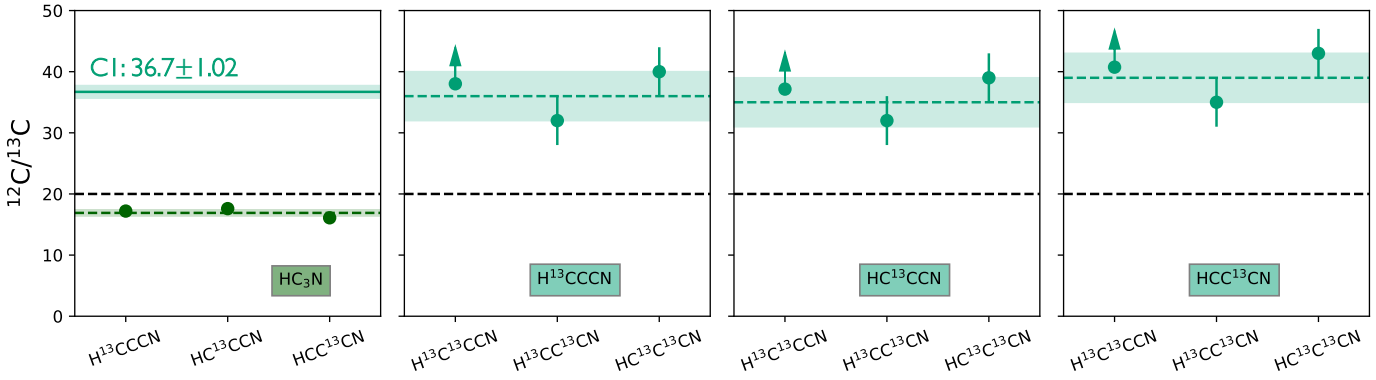

Fig. 4: Carbon isotopic ratios ($^{12}C/^{13}C$) measured for different isotopologues of HC_3N toward G+0.693 (C1 component) in the Galactic center. From left to right, the panels show the ratios obtained with HC_3N, $H^{13}CCCN$, $HC^{13}CCN$, and $HCC^{13}CN$ in the numerator. The black dashed horizontal lines indicate the canonical Galactic center value of ∼20. The points with arrows denote lower limits, and the scatter points with error bars represent individual measurements. Light green corresponds to ratios derived from double-isotopologues, while olive green corresponds to ratios from the main isotopolog. In each panel, the dashed green line and shaded area indicate the average value and uncertainty for that molecule. Moreover, in the first panel, the solid light green line and shaded area shows the average ratio derived from the double isotopologues.

describing the molecular emission were obtained using the automatic fitting routine `AUTOFIT`, which performs a nonlinear least-squares LTE optimization based on the Levenberg–Marquardt algorithm (Martín et al. 2019a).

The free parameters considered in the `MADCUBA` fit are the column density of the molecule (N), the excitation temperature (T_{ex}), the velocity (v_{LSR}), the full width at half maximum (FWHM) and the source size (θ_{source}). As determined in Colzi et al. (2024), we considered component C1 to be extended for the line fitting, meaning that no beam dilution was applied, while for C2, we used a source size[4] of 9″. The FWHM of the C1 component of HC_5N has been left as a free parameter (as for HC_3N), while for C2 we assumed the same value as HC_3N to ensure convergence of the fit. For the ^{13}C-isotopologues, the FWHM has been fixed to that of the same component of the main isotopolog. T_{ex} and v_{LSR} were left free in the fitting procedure unless their relative errors were higher than 15%. In the latter case, these parameters were also fixed to the values of the other isotopologues used to derive the $^{12}C/^{13}C$ ratio or, when possible, to the average value of similar species. The final column densities were derived using the antenna temperature (T_A^*) scale for the C1 component and the main beam temperature (T_{MB}) scale for the C2 component, which has been found to be a compact condensation (Colzi et al. 2024). T_{MB} was obtained from T_A^* using the formula $T_A^* = T_{MB}\,\eta_{MB}$,

[4] This explains the diverging evolution of the modeled line intensities for the C1 and C2 components with increasing J observed in Figs. 1 and A.1. Specifically, the intensities of higher J transitions become more prominent as the coupling between the source size and the telescope beam improves at higher frequencies.

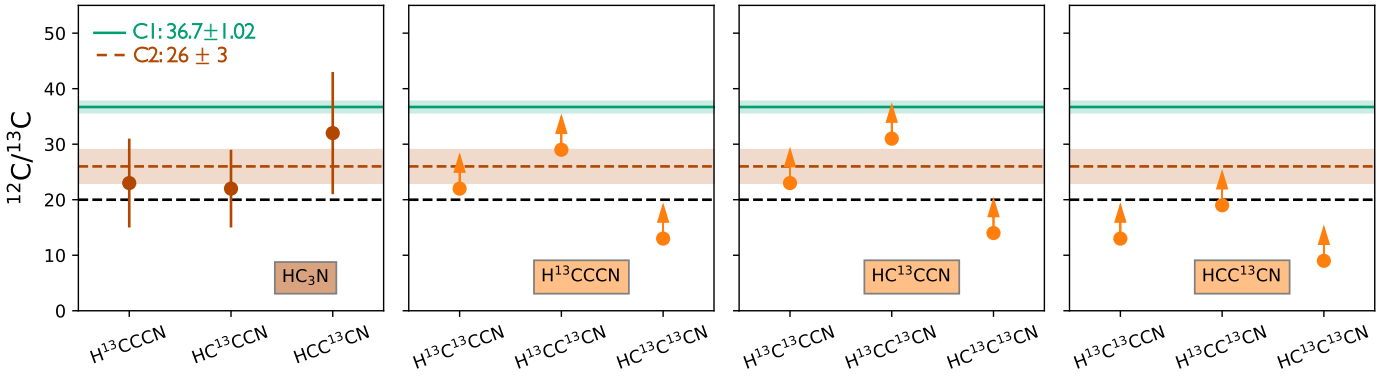

Fig. 5: Same as Fig. 4, but for C2. The black dashed horizontal lines indicate the canonical Galactic center value of ~20. The light orange arrows indicate the lower limits on the ratios derived from the double isotopologues, while dark orange corresponds to those derived from the main isotopolog. The dashed dark orange line and shaded region in all panels represent the average value and its uncertainty derived from the measurements shown in the first panel. The average value obtained for C1 is also shown as a solid light green line with its corresponding shaded region for the error (as in the first panel of Fig. 4).

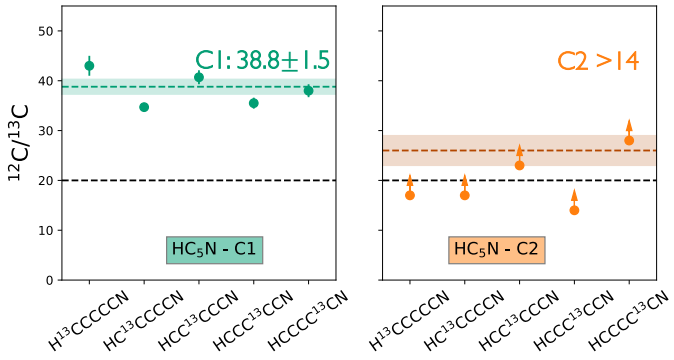

Fig. 6: $^{12}C/^{13}C$ ratios derived from HC_5N for the C1 component (left panel) and the C2 component (right panel). In both panels the black dashed horizontal lines indicate the canonical Galactic center value of ~20. In the left panel, the light green dashed line and shaded region indicate the average value and its uncertainty derived from HC_5N. In the right panel, the dark orange line and shaded region show the average value obtained for C2 from HC_3N, illustrating that the lower limits derived from HC_5N are consistent with this value.

where η_{MB} is the ratio of the main beam efficiency, B_{eff}, and the forward efficiency of the telescope,[5] F_{eff}.

When one of the isotopologues was not detected, we derived an upper limit to its column density. These limits were estimated using 3 × rms at the corresponding rest frequency, together with the assumed excitation temperature (T_{ex}) and linewidth (FWHM) (see Table C.1). For the C2 component of the double ^{13}C isotopologues we computed several upper limits because the adopted T_{ex} depends on which single ^{13}C isotopolog is taken as reference. This procedure ensures that the resulting lower limits on the $^{12}C/^{13}C$ isotopic ratios are derived consistently and accurately. The only exception is the column density derived for $H^{13}C^{13}CCN$ (Fig. A.2). Two of its transitions are slightly blended with emission from other species, preventing a reliable fit. For this reason, we provide an upper limit obtained by manually increasing N until the synthetic spectrum reproduced the full observed line profile. The best LTE fits are shown superimposed on the observed spectra in Figs. 1–3, A.1–A.6, B.1, and B.2. The corresponding fitting results are summarized in Table C.1.

From the derived total column densities, we calculated the $^{12}C/^{13}C$ ratios in two ways: (i) by dividing the column density of the main isotopolog by those of the single ^{13}C isotopologues (for both HC_3N and HC_5N), and (ii) for HC_3N only, by dividing the single ^{13}C isotopologues by the double ^{13}C isotopologues, considering all possible combinations. The resulting isotopic ratios are reported in Tables 2 and 3, for HC_3N and HC_5N respectively, and are graphically presented in Figs. 4, 5, and 6.

For the C1 component of HC_3N, the $^{12}C/^{13}C$ ratios derived from the main isotopolog are approximately factor of two lower than those obtained from double-^{13}C species. This discrepancy likely stems from moderate optical depth in the HC_3N lines ($\tau \sim 0.1$–0.5) and a lack of sufficiently optically thin transitions to constrain the opacity, which is a lower limit. Consequently, also the column densities derived from the main isotopolog should be treated as lower limits. In fact, the optically thinnest lines are all in the high-J group, where τ ranges only from 0.001 to 0.04. Furthermore, we have assumed that the emitting gas is more extended than the telescope beam; if this is not the case, the derived opacities would represent lower limits. It should be noted that, if the HC_3N column density of the C1 component is increased to reproduce the $^{12}C/^{13}C$ ratio derived from the double isotopologues, a source size of $\gtrsim$25–30″ would be required to match the observed spectra. In this case τ would be better constrained, reaching values up to 2–3. In contrast, the source size is constrained for the C2 component, and even though some transitions are optically thick, we were able to apply reliable opacity corrections to the final column densities (with τ between 0.1 and 2.5). An additional indication of optical depth effects in C1 is that the T_{ex} derived for the main isotopolog is lower than, and inconsistent with, the excitation temperature of the optically thin ^{13}C isotopologues, whereas in C2 the T_{ex} values agree within the uncertainties. Based on these considerations, we conclude that the most reliable isotopic ratio for the C1 component of HC_3N is that derived from the double ^{13}C isotopologues, which yields an average value of 36.7±1.02. For the C2 component, the ratio

[5] The beam efficiencies of the telescopes are available online at `https://publicwiki.iram.es/Iram30mEfficiencies` and `https://rt40m.oan.es/rt40m_en.php` for the IRAM 30m and Yebes 40m telescopes, respectively.

Table 2: Column densities and isotopic ratios for HC_3N.

Molecule	Comp.	N ($\times10^{14}$ cm^{-2})	$^{12}C/^{13}C$
HC_3N^a	C1	6.54±0.07[g]	
	C2	9±3	
$H^{13}CCCN$	C1	0.380±0.004	17.2±0.3
	C2	0.39±0.04	23±8
$HC^{13}CCN$	C1	0.372±0.007	17.6±0.4
	C2	0.41±0.05	22±7
$HCC^{13}CN$	C1	0.407±0.006	16.1±0.3
	C2	0.27±0.04	32±11
$H^{13}C^{13}CCN$	C1	<0.01	>38 / >37 / >40[b]
	C2	<0.018[c]	>22 / >23[d]
	C2	<0.022[e]	>13[f]
$H^{13}CC^{13}CN$	C1	0.0117±0.0014	32±4 / 32±4 / 35±4[b]
	C2	<0.013[c]	>28 / >30[d]
	C2	<0.015[e]	>19[f]
$HC^{13}C^{13}CN$	C1	0.0095±0.0010	40±4 / 39±4 / 43±4[b]
	C2	<0.029[c]	>13 / >14[d]
	C2	<0.032[e]	>8[f]
Average values C1[h]			
HC_3N/single ^{13}C			16.9±0.5
$H^{13}CCCN$/double ^{13}C			36±4
$HC^{13}CCN$/double ^{13}C			35±4
$HCC^{13}CN$/double ^{13}C			39±4
Mean of double isotopologues			36.7±1.02
Average value C2			
HC_3N/single ^{13}C			26±3

Notes. [(a)] Taken from Colzi et al. (2024). Only the low-J transitions are included in the results of this paper. [(b)] Relative to $H^{13}CCCN$ / $HC^{13}CCN$ / $HCC^{13}CN$. [(c)] Calculated using the same T_{ex} of the single ^{13}C isotopologues $H^{13}CCCN$ and $HC^{13}CCN$ (see Table C.1). [(d)] Relative to $H^{13}CCCN$ / $HC^{13}CCN$. [(c)] Calculated using the same T_{ex} of the single ^{13}C isotopolog $HCC^{13}CN$ (see Table C.1). [(f)] Relative to $HCC^{13}CN$. [(g)] The fractional abundance of HC_3N relative to H_2 is $(4.8 \pm 0.7) \times 10^{-9}$, adopting an H_2 column density of $N(H_2) = 1.35 \times 10^{23}$ cm^{-2} from Martín et al. (2008), assuming an uncertainty of 15% of its value. [(h)] Average values are calculated as the arithmetic mean of the measurements $\bar{x} = (1/N) \sum_{i=1}^{N} x_i$, where x_i is the i-th measurement and N is the number of measurements, while their uncertainties $\sigma_{\bar{x}}$ are estimated from the data standard deviation $s = \sqrt{\frac{1}{N-1} \sum_{i=1}^{N} (x_i - \bar{x})^2} \rightarrow \sigma_{\bar{x}} = s/\sqrt{N}$.

derived from the main isotopolog is considered robust, giving a value of 26±3.

For HC_5N, for which only the C1 component is detected in the ^{13}C isotopologues, the main isotopolog is already optically thin ($\tau \sim 0.01$–0.03). Consequently, the $^{12}C/^{13}C$ ratios derived from the main species are considered reliable. We also note that, in this case, the excitation temperatures obtained for the main and the ^{13}C isotopologues are mutually consistent. The final isotopic ratio, computed as the average over all possible isotopolog combinations, is 38.8±1.5.

The average isotopic ratio derived from HC_3N and HC_5N is 37.7±1.0, which is higher than the values reported from gas-phase molecular emission in the Galactic center prior to 2020. As we discuss in Sect. 4.1, more recent studies employing methods

Table 3: Column densities and isotopic ratios for HC_5N.

Molecule	Comp.	N ($\times10^{14}$ cm^{-2})	$^{12}C/^{13}C$
HC_5N^b	C1	1.247±0.018[a]	
	C2	1.7±0.3	
$H^{13}CC_4N$	C1	0.0288±0.0013	43±2
	C2	<0.098	>17
$HC^{13}CC_3N$	C1	0.0355±0.0005	35.1±0.7
	C2	<0.098	>17
$HC_2^{13}CC_2N$	C1	0.0302±0.0010	41.2±1.4
	C2	<0.075	>23
$HC_3^{13}CCN$	C1	0.0347±0.0010	35.9±1.1
	C2	<0.124	>14
$HC_4^{13}CN$	C1	0.0324±0.0010	38.5±1.3
	C2	<0.060	>28
Average value C1			
HC_5N/single ^{13}C			38.8±1.5

Notes. [(a)] The fractional abundance of HC_5N relative to H_2 is $(9.2 \pm 1.4) \times 10^{-10}$, adopting an H_2 column density of $N(H_2) = 1.35 \times 10^{23}$ cm^{-2} from Martín et al. (2008), assuming an uncertainty of 15% of its value. [(b)] Only the low-J transitions are included in the results of this paper.

less affected by the lines opacity of the main isotopologues have obtained ratios consistent with those found here. Altogether, these results indicate that the $^{12}C/^{13}C$ ratio in the CMZ is likely higher than the commonly adopted value of 20.

3.2. Astrochemical modeling of isotopologues

In this section, we investigate the possible effects of isotopic fractionation on the derived $^{12}C/^{13}C$ ratio. We employ the chemical model developed by Sipilä et al. (2023), which incorporates an updated chemical network including all combinations of ^{13}C-, ^{15}N-, and $^{13}C^{15}N$-bearing molecular species, together with the most recent low-temperature isotopic exchange reactions. This chemical network includes ^{13}C in molecules with up to 3 C atoms. This means that the fractionation of larger precursors of HC_3N and HC_5N, such as C_4H, is not treated. Thus, we have first analyzed the primary chemical pathways responsible for the formation of HC_3N, and subsequently investigate the $^{12}C/^{13}C$ ratio of its main precursor species. We have performed two models, for the two gas components C1 and C2, respectively. In particular, we have assumed as gas kinetic temperatures, T_{kin}, and H_2 densities, n_{H_2}, those reported in Table 1, which remain constant throughout the simulation. We have also assumed a dust temperature, T_{dust}, of 20 K, as typically found in the CMZ (e.g., Rodríguez-Fernández et al. 2004; Henshaw et al. 2023; Battersby et al. 2025). Moreover, we have used a cosmic-ray ionization rate of 1.3×10^{-15} s^{-1}, as estimated for G+0.693 (Rivilla et al. 2022; Sanz-Novo et al. 2024). Finally, because of the high column densities of gas present in the CMZ, the G+0.693 molecular cloud is highly shielded from external ultraviolet photons, and then we have assumed a visual extinction, A_V of 40 mag. The rest of the model parameters are assumed the same as in Sipilä et al. (2023). The initial elemental abundances are those used in Jiménez-Serra et al. (2018). In the following, we study the chemistry up to 10^5 yr, as previous works have shown that the molecular abundances observed toward G+0.693

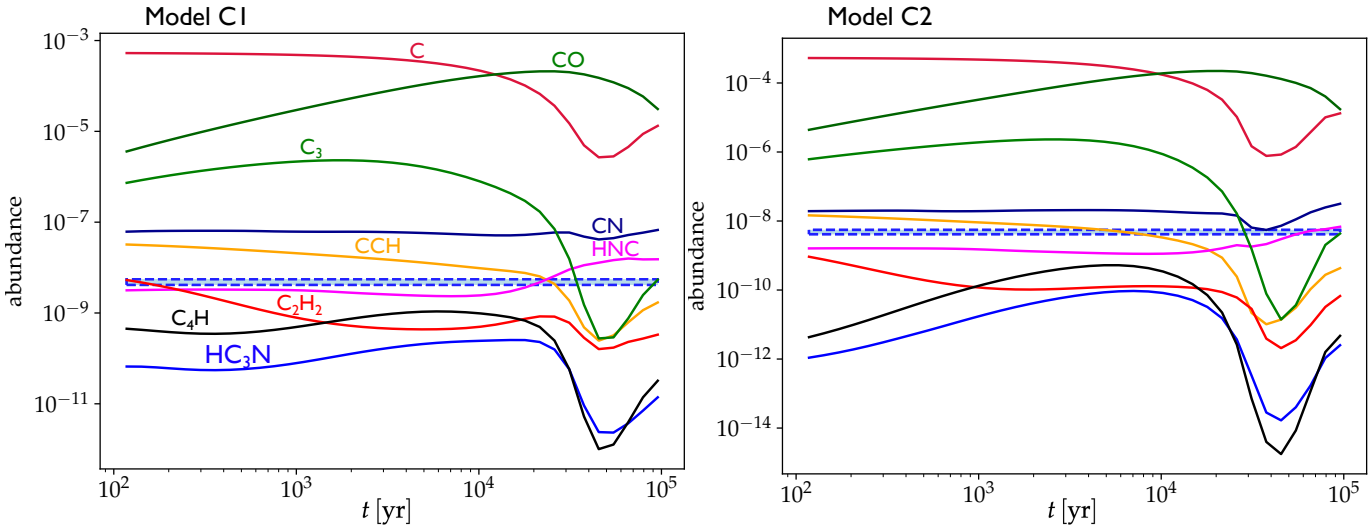

Fig. 7: Time evolution of the simulated abundances (relative to H_2) of HC_3N and its main precursor species for the two physical models considered in this work. The left and right panels show the results for the C1 and C2 components, respectively. In both panels the blue horizontal region represents the observed abundance toward the C1 component. The abundances are calculated using the chemical network of Sipilä et al. (2023) and adopting the physical parameters described in Sect. 3.2. The figure highlights that CCH, C, and C_3 are among the most abundant carbon-chain precursors at early times, enabling the formation of C_4H and subsequently HC_3N through the reaction C_4H + N. At later times, CN and HNC become increasingly important in the chemistry.

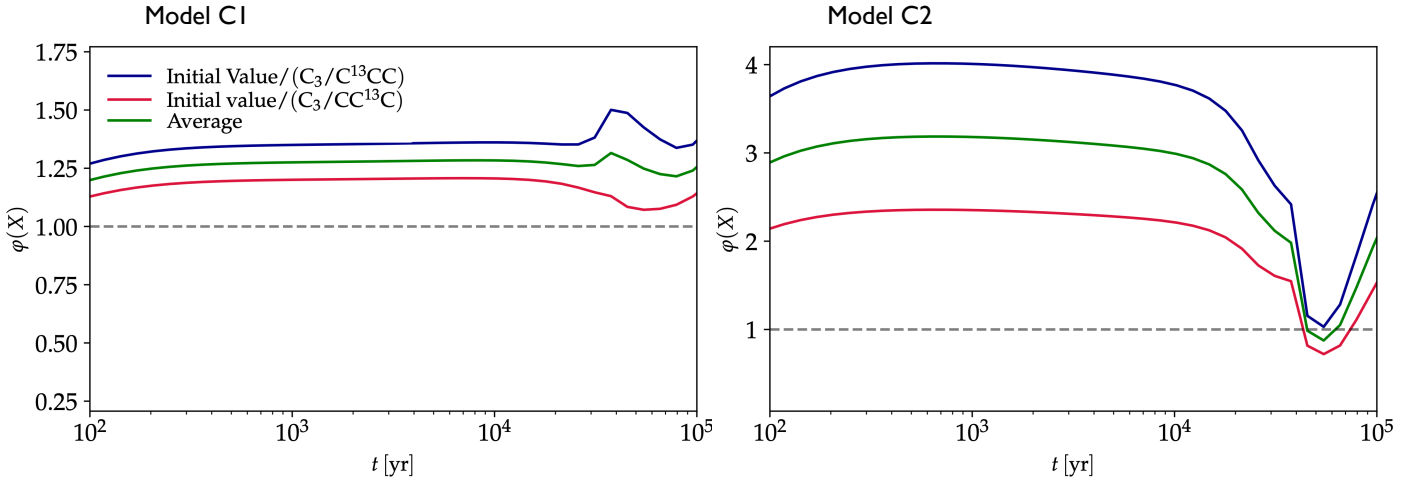

Fig. 8: Predicted isotopic fractionation degree, $\varphi(C_3)$, as a function of time for the two models. The quantity φ(X) is defined as the ratio of the initial elemental $^{12}C/^{13}C$ ratio to the modeled isotopic ratio for species X. In both panels the black dashed horizontal line represents φ(X)=1. The left panel shows the results for the model of C1, while the right panel corresponds to the model of C2. The curves represent the fractionation for the different ^{13}C substitutions in C_3, together with their average value. At early times ($\lesssim 3\times10^4$ yr), isotopic exchange reactions between ^{13}C and C_3 drive the fractionation degree toward values close to $e^{\Delta E/T}$, leading to moderate fractionation in the C1 model and stronger effects in the lower-temperature C2 model.

can be reproduced for an evolutionary time between 10^4 and 10^5 yr after the shock event (see, e.g., Requena-Torres et al. 2006; Sanz-Novo et al. 2024).

In Fig. 7 we show the simulated abundances of HC_3N and its main precursors, for the models of C1 and C2, respectively. The behavior in both models is very similar with up to an order of magnitude lower abundances for the low gas-phase temperature model C2. In both models we have found that the main formation pathway to form HC_3N at almost all timescales, up to ~3×10^4 yr, is through C_4H + N (see similar behavior in abundances in Fig. 7 and scheme in Fig. D.1). At 10^5 yr this reaction is responsible for 43% of HC_3N formation, followed by C_3N^- + H (24%), C_2H_2 + CN (10%), and CCH + HNC (7%), among other less important reactions. In general, C_4H is formed in the gas phase starting from the reaction CCH + C → C_3, followed by subsequent reactions involving C, H, H_2, and electrons. CCH, C, and C_3 are among the most abundant precursor species up to ~3×10^4 yr, whereas at later times HNC and CN become increasingly important. Overall, C_3 represents the final key precursor in the chemical formation pathway of HC_3N and can therefore be used to investigate the degree of its isotopic fractionation. It should also be noted that at these later timescales the main sink of atomic carbon is CO.

The fractional abundance of HC_3N relative to H_2 derived from observations is $(4.8 \pm 0.7) \times 10^{-9}$, calculated using the

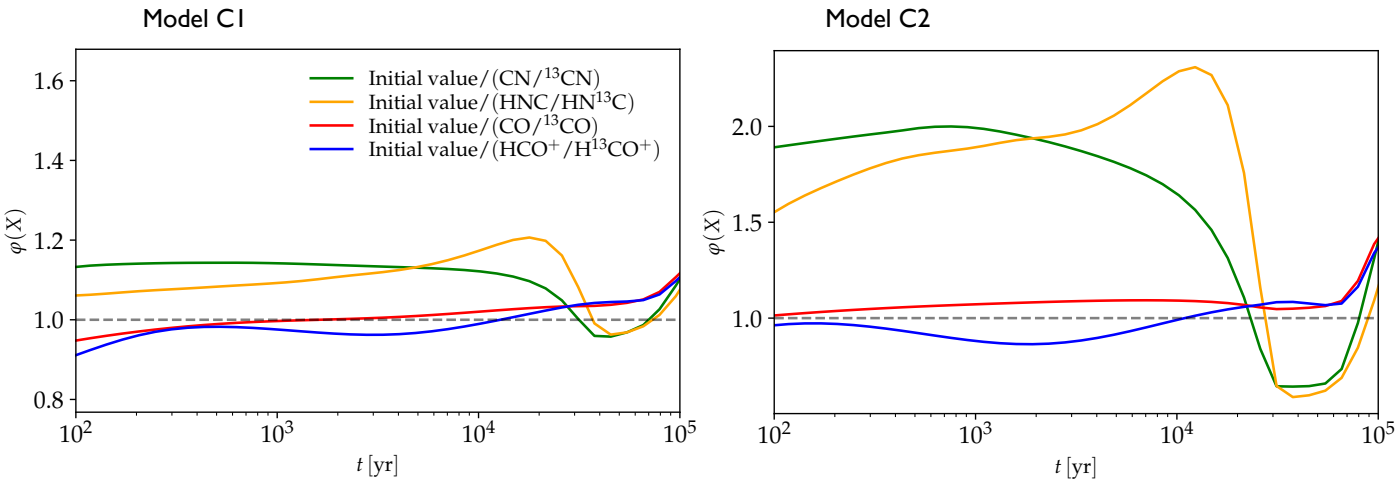

Fig. 9: Same as Fig. 8 but for CN, HNC, CO, and HCO^+ as a function of time for the models of C1 (left) and C2 (right). The fractionation degree decreases below unity at intermediate times, reflecting the role of CO and HCO^+ as the main sinks of ^{13}C in the gas phase. At later times, the increasing abundance of He^+ produced by cosmic rays leads to the reformation of atomic carbon and carbon chains, causing the fractionation degree to rise again toward values close to unity. These two species are therefore expected to be only weakly affected by isotopic fractionation over most of the chemical evolution.

HC_3N column density derived by Colzi et al. (2024) for C1 and adopting an H_2 column density of $N(H_2) = 1.35 \times 10^{23}$ cm^{-2} from Martín et al. (2008), assuming an uncertainty of 15% of its value. As shown in Fig. 7, this abundance cannot be fully reproduced by our models, with the closest value attained at approximately $2{\times}10^4$ yr. As discussed in Sect. 2.1, most of the molecules observed toward G+0.693 are likely formed following a major shock event caused by a cloud–cloud collision. Consequently, part of the missing HC_3N may reside on grain surfaces. Dutkowska et al. (2025) recently investigated the chemistry of typical CMZ sources, including shocked environments, and demonstrated that the HC_3N abundance observed in G+0.693 can be reproduced using a shock model with a cosmic-ray ionization rate of $\sim 10^{-15}$ s^{-1} (see their Figs. 2 and 4), consistent with values inferred from previous studies. These differing physical conditions could, in principle, influence the predicted isotopic ratios; therefore, they warrant a more detailed investigation in future dedicated works. In any case, sufficient time has elapsed since the shock event (between 10^4 and 10^5 yr; see, e.g., Requena-Torres et al. 2006; Sanz-Novo et al. 2024) for the gas-phase chemistry to reach a new equilibrium. Therefore, we do not expect significant deviations from the results obtained at comparable timescales, as explained below.

We now define the isotopic fractionation degree, φ(X), as the ratio between the initial elemental $^{12}C/^{13}C$ ratio and the predicted $^{12}C/^{13}C$ ratio for species X. We have tested that this quantity is independent of the initial value adopted in the model. Figure 8 presents $\varphi(C_3)$ averaged over its three possible isotopologues corresponding to the position of the ^{13}C atom. For C1, $\varphi(C_3)$ ranges between 1.2 and 1.3, while for C2 it spans values from 0.85 up to 3.2. These results are generally consistent throughout most of the chemical evolution with theoretical expectations based on the isotopic exchange reactions $^{13}C + C_3 \rightarrow {}^{12}C + C^{13}CC/{}^{13}CCC/CC^{13}C$, which are exothermic by $\Delta E = 43$ K, 27 K, and 27 K, respectively (e.g., Colzi et al. 2020; Loison et al. 2020). These reactions proceed efficiently as long as C_3 remains abundant, that is, at times earlier than $\sim 3{\times}10^4$ yr, causing the fractionation degree $\varphi(C_3)$ to approach $e^{\Delta E/T_{\rm kin}}$, where $T_{\rm kin}$ is the kinetic temperature of the gas (see Table 1). For C1, this yields expected values of 1.36 and 1.21 for the $C^{13}CC$ and ^{13}CCC isotopologues, respectively, while for C2 the corresponding values are 4.19 and 2.45 for $C^{13}CC$ and ^{13}CCC. This is consistent with what is illustrated in Fig. 8, which shows that for timescales shorter than $\sim 3{\times}10^4$ yr the predicted $\varphi(C_3)$ values for $C^{13}CC$ and ^{13}CCC are close to the theoretical values discussed above.

At timescales longer than $\sim 3{\times}10^4$ yr, we investigate the isotopic fractionation degree of CN and HNC, which also become increasingly important for the formation of HC_3N. As shown in Fig. 9, both φ(CN) and φ(HNC) drop below unity, reaching values as low as $\sim$ 0.6 in the low-temperature C2 model. At later times, the fractionation degree increases again, approaching values of 1.2–1.3 at 10^5 yr. This behavior was previously reported by Colzi et al. (2020) for models with a high cosmic-ray ionization rate and arises because CO and HCO^+ act as the main sinks of ^{13}C during this phase. At longer times, as the abundance of He^+ produced by cosmic rays increases, atomic carbon and carbon chains are re-formed, and their isotopic fractionation degree returns to higher values comparable to those at earlier times. These effects are more pronounced in the low-temperature model. Even if not affecting the fractionation degree of HC_3N, it is worth noting that for the shorter timescales CN and HNC are enhanced in ^{13}C because of the isotopic exchange reactions (4) and (25) listed in Table 1 by Sipilä et al. (2023). Similar conclusions apply to HC_5N, which is mainly formed from C_3 and CN, as illustrated in the scheme in Fig. D.2 in Appendix D.

Considering the fractionation degrees predicted by our models for C1 and C2, the observed values for the two gas components indicate low to intermediate fractionation degree at times earlier than 3×10^4 yr[6] (1.28 and 3.15 for C1 and C2, respectively). Under these conditions, we have multiplied the observed ratios with the corresponding isotopic fractionation degree and we have found that the initial $^{12}C/^{13}C$ for the parental material of molecular clouds in the CMZ is constrained to lie in the range 48–82, with the higher values inferred for C2 when only average estimates are considered. However, when the uncertainties on the $^{12}C/^{13}C$ obtained for C2 component are taken into account,

[6] We do not consider later timescales because the HC_3N abundance decreases to unrealistically low values ($< 10^{-11}$), see Fig. 7.

the inferred initial ratio may be as low as 15×3.15=47 (see Table 2), making it compatible with a lower-end initial elemental $^{12}C/^{13}C$ ratio of 48 for both components. Conversely, we cannot exclude significantly higher values; the 1σ upper bond of the C2 average (31±11 individually, or 26±3 in the ensemble) suggests an initial ratio reaching as high as ∼98, potentially overlapping with ratios measured in the local Galaxy (see Fig. 10). As the spectral features from which we inferred the $^{12}C/^{13}C$ ratio for C2 are partially blended with the main C1 component, the resulting estimates for C2 are subject to higher systematic uncertainty. Consequently, we adopt the value of 48 inferred from the more robust C1 component as the representative initial ratio for molecular clouds in the CMZ for the remainder of the paper. At later times, the models predict lower levels of isotopic fractionation, corresponding to possible initial $^{12}C/^{13}C$ values of 35–41 for C1 and 15–32 for C2. However, because the modeled HC_3N abundances approach the observed values more closely at earlier times, we do not consider these ratios further in our discussion. In future studies, molecules less affected by fractionation, such as CO and HCO^+, could be used to perform this type of analysis, as shown in Fig. 9.

4. Discussion

In this work we have derived a $^{12}C/^{13}C$ ratio of 48 toward G+0.693 in the CMZ, indicative of the initial value of the material from which this molecular cloud formed. This value is obtained from molecular species whose line emission is optically thin (single isotopologues of HC_5N and double isotopologues of HC_3N), and is corrected for isotopic fractionation effects using astrochemical models based on the most up-to-date chemical network including ^{13}C- and ^{15}N-isotopologues. In Sect. 4.1 we compare this result with $^{12}C/^{13}C$ ratio measured both in the Milky Way (CMZ and disk) and in extragalactic sources. Furthermore, the derived $^{12}C/^{13}C$ ratio can be used as probe of the origin of the gas, and the elements within it, in the CMZ (Sect. 4.2).

4.1. Comparison with other sources

4.1.1. Comparison with other CMZ sources

All measured $^{12}C/^{13}C$ ratios toward the CMZ are summarized in the left panel of Fig. 10. In the CMZ of the Milky Way, the $^{12}C/^{13}C$ isotopic ratio has been extensively investigated over the past five decades through radioastronomical observations. Measurements toward prominent molecular clouds such as Sgr B2 and Sgr A yield values ranging from ∼3 to 30 for relatively simple molecules (e.g., HC_3N, H_2CO, OCS, HCO^+, HCN, HNC, C_3, and CH), based on both absorption and emission lines (e.g., Turner 1991; Giesen et al. 2020b). Higher ratios, typically ∼20–32, have been derived from COMs, including CH_3OH, CH_3CN, CH_3CH_2OH, C_2H_3CN, and C_2H_5CN. Most of these determinations rely on direct comparisons between the line intensities of a main isotopolog and its ^{13}C-substituted counterpart. However, this approach is strongly affected by optical depth effects and therefore generally provides lower limits to the true isotopic ratio. Notably, values derived from COMs tend to lie at the upper end of the observed range, likely because their transitions are typically more optically thin than those of simpler species (e.g., Halfen et al. 2017), or because they trace different gas components, such as warmer and denser gas located closer to the protostar.

More reliable measurements based on optically thin tracers and double isotopolog methods have also been reported. For example, Humire et al. (2020) and Yan et al. (2023) derived the carbon isotopic ratio using $C^{34}S/^{13}C^{34}S$ toward the +50 km s^{-1} cloud and the Sgr B2 line of sight, obtaining values between 22–35. These results are consistent with the higher end of previously reported values (see left panel of Fig. 10). In addition, Martín et al. (2012) derived ratios of 15–45 toward the circumnuclear disk around Sgr A*, using CN and correcting for line opacity effects through its hyperfine structure. Jones et al. (2012) found that integrated intensity ratios between ^{12}C- and ^{13}C-bearing isotopologues of HCN, HCO^+, and HNC are typically significantly lower than 24, confirming that emission from the main isotopologues is generally optically thick in the CMZ. However, they also identified regions at the most redshifted velocities (∼100 km s^{-1}) where the $^{12}C/^{13}C$ ratio derived from HCO^+ reaches values as high as 45. Consistently, Riquelme et al. (2010) reported $^{12}C/^{13}C$ ratios >40–70 in the external disk–halo interface of the CMZ, suggesting the presence of infalling less processed, more pristine material from a nucleosynthesis perspective.

In this work, we derive a ratio of ∼37 using HC_5N and the double isotopolog of HC_3N, and up to 48 when correcting for fractionation effects. Moreover, using the column densities reported by Colzi et al. (2022a), considering $HC^{15}N$ and $H^{13}C^{15}N$, we derive a $^{12}C/^{13}C$ ratio of ∼36 (not corrected for fractionation) toward the C1 component of G+0.693. More recently, Luo et al. (2024) derived $^{12}C/^{13}C$ ratios higher than 35 from absorption-line observations toward Galactic center region lines of sight (R_{GC} ∼ 1 kpc). Finally, Boogert et al. (2000) used ISO-SWS ice observations toward the Galactic center source GC3 and obtained a $CO_2/^{13}CO_2$ ratio of 52 ± 11. These results further support the presence of a $^{12}C/^{13}C$ ratio of at least ∼35 toward the CMZ and highlight the importance of employing optically thin tracers, as well as considering fractionation effects, for accurate determinations.

4.1.2. Comparison with Milky Way sources

The right panel of Fig. 10 compiles the most relevant $^{12}C/^{13}C$ measurements obtained in molecular clouds across the Galactic disk and in the CMZ. For the comparison with Galactic sources, we revised the adopted galactocentric distances to ensure consistency with the most recent determinations. For H_2CO, CS, CO, and CN, we adopted the updated distances reported by Yan et al. (2019, 2023) , which use trigonometric parallaxes when available and revised kinematic distances otherwise. The only exception is WB89-437, for which Wouterloot & Brand (1996) derived a $^{12}CO/^{13}CO$ ratio of 104 ± 60; for this source we adopted the trigonometric parallax distance of 13.24 kpc determined by Hachisuka et al. (2015). For CH^+ and CH, we used the galactocentric distances reported by Ritchey et al. (2011) and Jacob et al. (2020), respectively. The majority of the sources in the disk lie at galactocentric distances R_{GC} between ∼2.5 and 11 kpc. The data include observations obtained with different molecular tracers; the molecules used and the corresponding references are listed in the figure and in Sect. 4.1. On average, the $^{12}C/^{13}C$ increases with galactocentric distance. This behavior is also consistent with the most recent Galactic chemical evolution models (Colzi et al. 2022b).

A linear regression fit including all the measurements yields the following galactocentric gradient when the CMZ data points are included:

$$^{12}C/^{13}C = (18 \pm 3) + (6.5 \pm 0.5)\, R_{GC}. \quad (1)$$

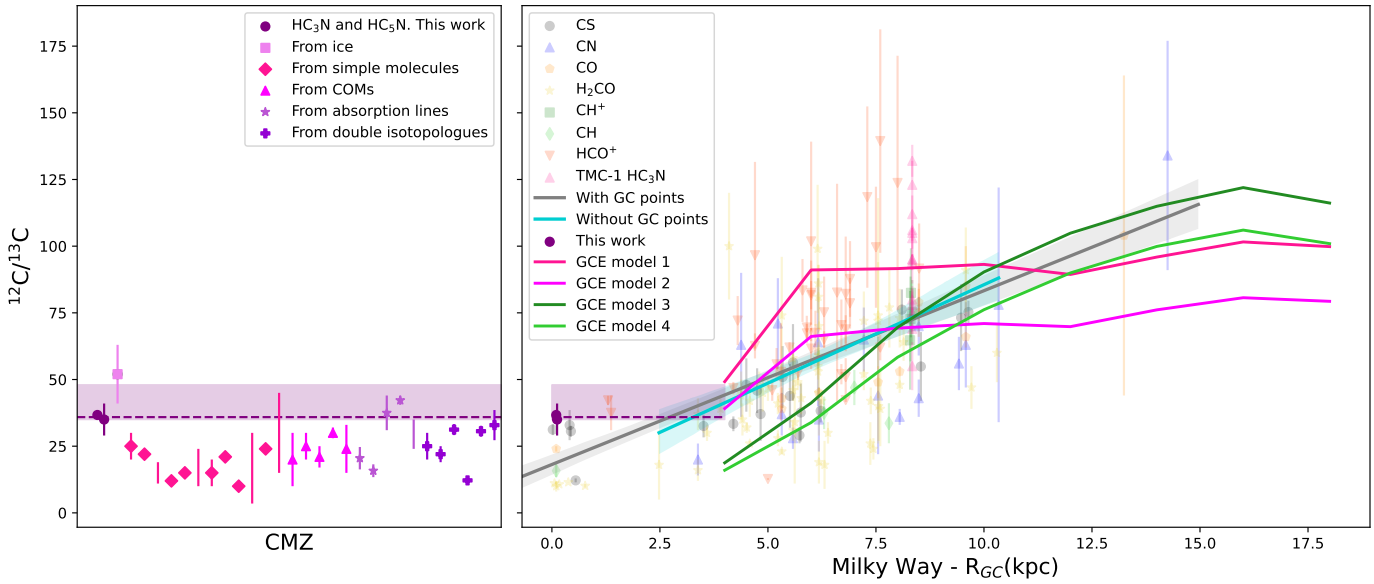

Fig. 10: $^{12}C/^{13}C$ ratios measured in the CMZ (left panel) and across the Galactic disk (right panel). In both panels, the purple dashed line indicates the value derived in this work (∼37), while the shaded region represents the range of values obtained when isotopic fractionation effects are taken into account. In the right panel, this line is extended to 4 kpc for comparative purposes. In the left panel, all the sources are within galactocentric distances of 20 pc and 1.3 kpc. The lines without symbols indicate the parameter ranges reported in the literature; the individual measurements are shown as symbols. Those measurements are taken from the literature, including values derived from ice observations (Boogert et al. 2000); from simple molecules (Fomalont & Weliachew 1973; Wannier & Linke 1978; Gardner & Whiteoak 1979; Goldsmith & Linke 1981; Gardner & Whiteoak 1982; Guesten et al. 1985; Langer & Penzias 1990; Turner 1991; Jones et al. 2012; Riquelme et al. 2010; Martín et al. 2012; Yan et al. 2019); from complex organic molecules (COMs) (Müller et al. 2008; Belloche et al. 2013; Müller et al. 2016; Margulès et al. 2016; Halfen et al. 2017); from absorption lines (Giesen et al. 2020b; Jacob et al. 2020; Humire et al. 2020; Luo et al. 2024); and from double-isotopolog methods (Humire et al. 2020; Yan et al. 2023). In the right panel, the literature measurements are derived using $C^{18}O$ (Langer & Penzias 1990; Wouterloot & Brand 1996; Keene et al. 1998), CN (Savage et al. 2002; Milam et al. 2005), CS (Yan et al. 2023), H_2CO (Henkel et al. 1980, 1982, 1983, 1985; Yan et al. 2019), CH^+ (Ritchey et al. 2011), CH (Jacob et al. 2020), and HCO^+ (Luo et al. 2024). Moreover, the values derived from different HC_3N isotopologues toward TMC-1 are taken from Tercero et al. (2024). This panel also includes Galactic chemical evolution (GCE) model predictions from Colzi et al. (2022b). Linear fits to the observational data, including and excluding Galactic center sources, are shown as gray and cyan solid lines, respectively, with their corresponding shaded confidence regions.

Excluding the Galactic center and R_{GC} >12 kpc sources results instead in the relation

$$^{12}C/^{13}C = (12 \pm 7) + (7.4 \pm 1.1)\, R_{GC}. \quad (2)$$

These trends are consistent with the observational trend obtained in previous works (see references in caption of Fig. 10) and with the predictions of Galactic chemical evolution models for the Milky Way (e.g., Romano et al. 2019; Romano 2022; Colzi et al. 2022b, see also right panel of Fig. 10).

Using the two reported linear relations for the Galactic gradient of the $^{12}C/^{13}C$ ratio, we estimate the galactocentric distances at which the observed values in this work, between 37 and 48, are expected. For the first relation taking into account CMZ sources this interval corresponds to $R_{GC} \approx 2.9-4.6$ kpc when using the central values of the coefficients. Similarly, adopting the second relation, excluding CMZ and outer Galaxy sources, the same range of isotopic ratios is obtained at $R_{GC} \approx 3.4-4.9$ kpc. Therefore, both gradients consistently indicate that $^{12}C/^{13}C$ ratios between 37 and 48 are most likely found at galactocentric distances of approximately $R_{GC} \sim 3-5$ kpc. When accounting for the uncertainties in the slopes and intercepts, this range broadens to roughly $R_{GC} \sim 2.1-6.8$ kpc. It should also be noted that the values obtained by Luo et al. (2024) at ∼ 1 kpc along the line of sight toward the CMZ are consistent with the values derived in our work within 100 pc of the Galactic center.

Moreover, in the Galactic disk the values obtained at a given R_{GC} the values obtained are not consistent among them. In fact, they are obtained using observations toward sources with different physical conditions and different molecules, pointing out also in this case the importance of taking into account isotopic fractionation, through astrochemical models, to properly retrieve the initial isotopic ratios of those regions of the Galaxy. For example, locally at 8.2 kpc, different $^{12}C/^{13}C$ ratios have been evaluated toward the cyanopolyyne peak in TMC-1. Tercero et al. (2024) reported that most of the ^{13}C resides in $HCC^{13}CN$ rather than in $H^{13}CCCN$ or $HC^{13}CCN$. In that region, the cosmic-ray ionization rate is lower than in the CMZ (∼1.3×10^{-17} s^{-1}), making the reaction C_2H_2 + CN one of the most efficient formation routes for HC_3N. Given the low kinetic temperature of TMC-1 (10 K), CN is likely fractionated (Colzi et al. 2020), and its low $^{12}C/^{13}C$ can propagate into HC_3N via the aforementioned reaction, which proceeds efficiently only in the forward direction at such low temperatures. The differences in the observed ratios toward TMC-1 indicate that this reaction does not involve carbon exchange during formation. Consequently, $^{12}C/^{13}C$ values obtained both from the single and double isotopologues when in-

cluding H^{13}CCCN and HC^{13}CCN, which exhibit ^{12}C/^{13}C values within the range 78–105 (see right panel of Fig. 10), likely better represent the intrinsic isotopic ratio of the local TMC-1 molecular cloud. In contrast, our results toward G+0.693 show that the ^{12}C/^{13}C values are consistent within 1σ among the different ^{13}C isotopologues of HC_3N in both C1 and C2, in line with on average higher $T_{\rm kin}$. However, as mentioned above, proper chemical models are needed to interpret the results (see Sect. 3.2).

4.1.3. Comparison with external galaxies

In external galaxies, the ^{12}C/^{13}C ratio spans nearly an order of magnitude (Fig. 11). Values exceeding 100 are reported in luminous and ultraluminous infrared galaxies (LIRGs/ULIRGs), whereas starburst galaxies, active galactic nuclei (AGN), and normal spiral galaxies typically exhibit lower ratios. Such lower values are generally associated with systems that are not undergoing large-scale mergers. Early extragalactic measurements were primarily based on ^{12}CO and ^{13}CO. However, the main isotopolog is usually severely optically thick ($\tau > 3$; e.g., Young & Sanders 1986; Wiklind & Henkel 1990; Kruegel et al. 1990), often yielding ^{12}C/^{13}C ratios below 15. Thus, we do not discuss the ratios derived from CO further in this paper. Subsequent studies employing alternative tracers reported higher and likely more reliable values. Aalto et al. (1991a,b) derived a ratio of 35±5 toward the center of the LIRG NGC 3256 and >20 toward four merging ULIRGs. They proposed that the elevated intensity ratios reflect a reduction in the mean optical depth of molecular clouds, possibly due to tidal disruption or starburst activity triggered by the merger process. A more robust determination was presented by Henkel et al. (1993), who reported ^{12}C/^{13}C >30 within the central 500 pc of the starburst galaxy NGC 253 using CN, CS, and HNC. Similarly, Mauersberger & Henkel (1993) suggested that enhanced central ^{12}C/^{13}C ratios are most plausibly explained by the inflow of less chemically processed gas toward the nuclear region. Such inflows may be driven by galaxy interactions, mergers, or by the dynamical effects of a stellar bar (see Sect. 4.2). Consistent results were later obtained by Tang et al. (2019), who derived values of ∼40 in three nearby starburst galaxies using CN. They also proposed that gas inflow from the outer disk into the circumnuclear region (inner kpc), possibly mediated by the halo and bar, could explain the observed enhancements.

More recently, spatially resolved observations of the starburst galaxy M82 have revealed a gradient in the ^{12}C/^{13}C ratio along its major axis, with values of ∼40 in the inner regions (very similar to the values obtained in our work) increasing to ∼50–100 at 0.45 kpc from the center (Li et al. 2022). This trend may reflect reduced optical depth effects outside the central regions, as well as genuine nucleosynthesis variations, as discussed in the following section for the CMZ. The ALMA ALCHEMI large program has provided a complete astrochemical census of the inner 500 pc of the nearby starburst galaxy NGC 253. Using ACA data, Martín et al. (2021) derived ^{12}C/^{13}C ratios from a wide range of molecular species, including CO, C^{18}O, HCO$^+$, HCN, HNC, CN, CS, H_2CO, CCH, and HC_3N, among others. They found a huge spread of values, demonstrating that the inferred isotopic ratios depend both on the molecular tracer and on the spatial resolution of the observations (Fig. 11; see also Meier et al. 2015; Martín et al. 2019b). This result underscores the necessity of accounting for line optical depth effects, varying molecular spatial distributions, as well as possible fractionation effects when deriving isotopic ratios also in extragalactic environments.

The values discussed above generally correspond to measurements averaged over the inner central kiloparsec of these galaxies, making them directly comparable to those obtained in the CMZ of the Milky Way (Fig. 11). The ^{12}C/^{13}C ratio derived in this work is consistent with the values reported for starbursts, AGN, and spiral galaxies (excluding ratios derived from the optically thick CO lines), suggesting that similar gas processing and chemical enrichment mechanisms may operate across these environments, as discussed in Sect 4.2. However, this comparison should be taken with cautions since the values from extragalatic sources taken from the literature could be both affected by line opacity and isotopic fractionation effects (e.g., Viti et al. 2020).

Measurements toward the nearby dwarf galaxies, the Large Magellanic Cloud (LMC) and the Small Magellanic Cloud (SMC), show values > 20 (Boreiko & Betz 1991; Johansson et al. 1994; Wang et al. 2009), reaching up to 82 in more recent measurements based on CO_2 ice observations (De Marchi et al. 2025). Possible connections of the CMZ with these systems are also discussed in the next section, together with the implications for chemical nucleosynthesis evolution.

4.2. Implications of the carbon isotopic ratios for Galactic center evolution and stellar nucleosynthesis

4.2.1. Carbon isotopic ratios as probes of gas accretion in the Galactic center

In Sect. 4.1.2 we have discussed that comparison with the ^{12}C/^{13}C ratios derived in the Milky Way disk toward massive star-forming regions shows that the values obtained in this work toward the CMZ are similar to those at galactocentric distances of ∼3–5 kpc (see right panel of Fig. 10). This supports a scenario in which the CMZ is replenished by gas with isotopic ratios characteristic of larger galactocentric distances. This process can be explained by the presence of bars as one of the main mechanisms driving gas inflow from the Galactic disk toward the CMZ where the dense molecular gas accumulates (e.g., Gerhard 2011; Sormani & Barnes 2019; Tress et al. 2020; Henshaw et al. 2023). It can be noted that a part of this flow can also come from the halo, a roughly spherical region surrounding the Galaxy that contains hot ionized gas, dark matter, and some old stars, where the gas is less reprocessed. In fact, there are some evidences that unmixed stars within the halo present ^{12}C/^{13}C ratios higher than 40 (e.g., Molaro et al. 2023; Rizzuti et al. 2025). This inflow can occur through the infall of cooler gas clouds, large-scale accretion along filaments, or galactic fountains driven by supernova explosions in the galactic disk (e.g., Henley et al. 2010; Riquelme et al. 2010; Bish et al. 2019). If the CMZ is fed by gas coming from a few kpc out in the disk, its isotopic ratios can reflect those larger $R_{\rm GC}$ values rather than purely local nucleosynthesis.

Another possible mechanism is the past interaction of the Milky Way with dwarf galaxies. The Milky Way has undergone several merger events with dwarf galaxies during its evolution. A well-known example is the ongoing accretion of the Sagittarius dwarf spheroidal galaxy, whose tidal disruption has produced the Sagittarius stellar stream (Ibata et al. 1994; Majewski et al. 2003). In addition, analyses of stellar kinematics and chemical abundances from *Gaia* data have revealed evidence for a major ancient merger with a dwarf galaxy known as Gaia–Enceladus, which contributed significantly to the formation of the Galactic stellar halo (Helmi et al. 2018; Myeong et al. 2018; Berni et al. 2026). Such accretion events illustrate how external material can be incorporated into the Milky Way and potentially influence the chemical properties of its gas reservoir. In fact, dwarf galaxies typically exhibit lower metallicities and contain less chemically processed material than the Milky Way, which can modify iso-

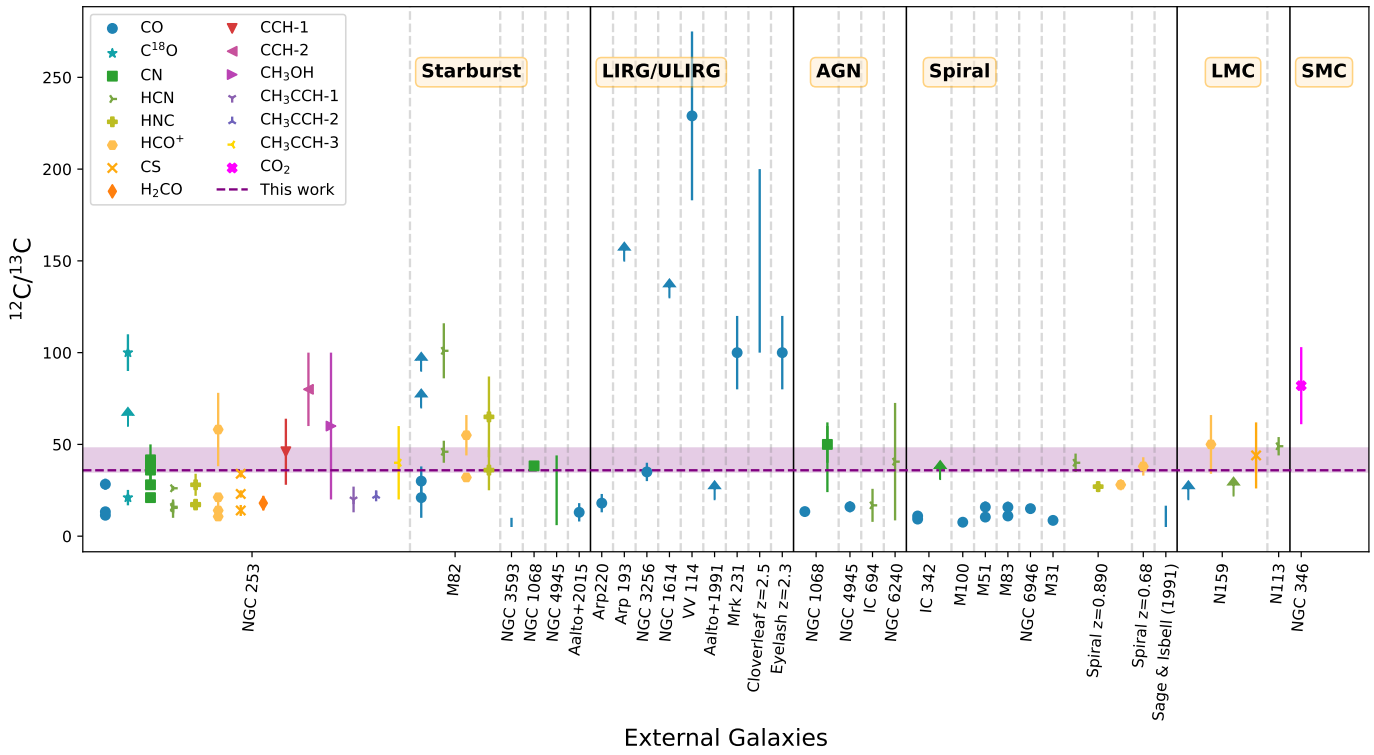

Fig. 11: $^{12}C/^{13}C$ ratios measured in external galaxies. The purple dashed line indicates the value derived in this work (~37), while the shaded region represents the range of values obtained when isotopic fractionation effects are taken into account. The lines without symbols indicate the parameter ranges reported in the literature; the individual measurements are shown as symbols. The values are taken from the literature, including values from starburst and spiral galaxies (Wiklind & Henkel 1990; Young & Sanders 1986; Encrenaz et al. 1979; Stark & Carlson 1984; Loiseau et al. 1990; Sage & Isbell 1991; Wiklind & Henkel 1992; Henkel et al. 1993; Aalto et al. 1995; Kikumoto et al. 1998; Muller et al. 2006; Martín et al. 2010; Henkel et al. 2014; Aladro et al. 2015; Wallström et al. 2016; Martín et al. 2019b; Tang et al. 2019; Martín et al. 2021; Li et al. 2022), from LIRGs/ULIRGs (Aalto et al. 1991a,b; Sliwa et al. 2013; Danielson et al. 2013; Sliwa et al. 2014; Henkel et al. 2014; Papadopoulos et al. 2014; Spilker et al. 2014), from AGN (Whiteoak et al. 1990; Solomon et al. 1990; Jiang et al. 2011; Aladro et al. 2013; Tang et al. 2019), from the LMC (Boreiko & Betz 1991; Johansson et al. 1994; Wang et al. 2009), and the SMC (De Marchi et al. 2025). The numbers in the legend correspond to the position of the ^{13}C in the molecule with respect to the C atoms.

topic ratios once this gas is accreted into the inner Galaxy. Recent work suggests that star formation in the inner Milky Way has occurred in several episodic bursts rather than continuously. Using Gaia color–magnitude diagram fitting, Ruiz-Lara et al. (2026) showed that super-metal-rich stars in the solar neighborhood, likely formed in the inner Galaxy and later migrated outward, trace multiple star formation episodes over the past ~ 13 Gyr, possibly triggered by satellite interactions and gas inflow events (see also Palla et al. 2024). After mixing within the Galactic halo or disk and subsequently migrating inward, such gas may increase isotopic ratios in the Galactic center, as observed here for carbon. This scenario is supported by the similarities between the isotopic ratios measured in the Large and Small Magellanic Clouds and those derived in this work (Sect. 4.1.3 and Fig. 11).

4.2.2. Some insights from stars and chemical evolution models of the CMZ

From the perspective of stellar nucleosynthesis, ^{12}C is predominantly synthesized via the triple-α process during the giant and supergiant phases of low-mass, intermediate-mass, and massive stars. In contrast, ^{13}C is primarily a secondary isotope produced through the CNO cycle and in nova outbursts. The enrichment of ^{13}C is largely dominated by long-lived asymptotic giant branch (AGB) stars and therefore occurs on longer timescales than the enrichment of ^{12}C. This difference in production channels naturally leads to a decrease in the carbon isotope ratio with increasing metallicity and decreasing R_{GC} across the Galactic disk. These trends are consistent with the predictions of Galactic chemical evolution models for the Milky Way disk (e.g., Romano et al. 2019; Romano 2022; Colzi et al. 2022b, see also right panel of Fig. 10). In this context, Galactic chemical evolution models provide an essential framework for interpreting isotopic ratios and their variation across different galactic environments. In particular, models that focus on the central regions of galaxies, including the CMZ of the Milky Way, aim to describe how processes such as gas inflow, star formation, stellar feedback, and mixing shape the chemical enrichment history of the nuclear regions (e.g., Spitoni et al. 2026). In fact, all of these are processes that could explain the high $^{12}C/^{13}C$ ratio of 48, typical of less processed material, inferred for the CMZ from this work.

Chemical evolution models focusing on the central zones of our Galaxy can only be constrained by a few measurements toward stars. For example, Kovtyukh et al. (2019, 2022) measured from Cepheids [Fe/H]<0.4 dex in the CMZ with a decrease in the inner 2 kpcs from 0.4 dex to solar 0 dex value. In general,

stars in the Nuclear Stellar Disk (NSD), the stellar counterpart of the CMZ, present solar or slightly higher metallicity (see also Najarro et al. 2009; Ryde & Schultheis 2015; Schultheis et al. 2019; Thorsbro et al. 2020; Matsunaga et al. 2023). These measurements further support the idea of a possible inflow of less reprocessed and low-metallicity gas in the central Galaxy. Going at smaller scales Chen et al. (2023) measured [Fe/H]∼0.5 dex or less in the inner 1.5 pc in the Nuclear Star Cluster (NSC) in the vicinity of the supermassive black hole. In fact, the sub-solar [Fe/H] stars have spatial anisotropy indicating a recent star cluster infall event, as well as they have different kinetics from the super solar-ones (Feldmeier-Krause et al. 2020; Do et al. 2020). They suggested that this is consistent with an infall of a globular cluster or of a dwarf galaxy.

From the point of view of models, Grieco et al. (2015) studied the chemical evolution of the NSD and compared with α-elements and Fe abundances of M giant stars by Ryde & Schultheis (2015). They suggest that the Galactic center experienced a rapid early formation phase with a high star formation efficiency ($\sim 25\,\mathrm{Gyr}^{-1}$) and an Initial Mass Function (IMF) richer in massive stars than the standard solar-neighborhood IMF (e.g., Kroupa et al. 1993), with the Chabrier 2003 IMF providing a better match to observations). The present-day star formation rate could be explained by a secondary burst triggered by a modest gas infall episode 0.5 Gyr ago, likely associated with bar-driven accretion, without significantly affecting the abundance patterns or the metallicity distribution function.

A more recent study by Friske & Schönrich (2025) further investigated the chemical evolution of nuclear stellar disks using analytical multi-zone models tailored to the central regions of barred galaxies. Their work explores how sustained gas inflow toward the Galactic center can shape the metallicity distribution and abundance patterns observed in NSDs. They find that continuous or recurrent gas accretion from the outer parts of the galaxy into the nuclear region, likely driven by the Galactic bar, can sustain star formation over extended periods while progressively enriching the interstellar medium. In this scenario, the NSDs are not formed in a single early episode but rather through prolonged star formation fueled by inward gas transport, yielding the metallicities and complex abundance trends usually observed in nuclear stellar populations.

Recent constraints on the chemical composition of the NSD were provided by Thorsbro et al. (2020), who analyzed high-resolution near-infrared spectra of M giant stars in the nuclear region. They found a predominantly metal-rich population, with metallicities up to [Fe/H] $\sim$ +0.5, and α-element abundances indicating a complex enrichment history. By comparing their measurements with chemical evolution models of the Galactic center by Grieco et al. (2015), they argued that the observed abundance patterns are consistent with rapid early enrichment (mini-starburst activity) followed by a more recent starburst $\sim$ 1 Gyr ago, involving accretion of primordial or slightly enriched gas. To trigger this starburst episode, the gas must be accreted either from other regions of the Galaxy or from extragalactic origin. This mini-starburst scenario is further supported by our findings, as the isotopic ratios we derive toward G+0.693 closely resemble those measured in starburst galaxies.

More recently, Spitoni et al. (2026) presented a new chemical evolution model for the NSD within a Bayesian framework. In this work, the authors explored scenarios in which the NSD forms primarily from gas transported to the Galactic centre through bar-driven inflows from the inner disk. By comparing model predictions with the observed metallicity distribution function and α-element abundance ratios, they showed that a simple inner-disk origin struggles to reproduce the metal-poor tail of the data. Models including additional dilution from more metal-poor gas, or alternatively adopting a low star formation efficiency combined with mild galactic winds, provide a better agreement with the observations, although the results depend on the level of bulge contamination in the stellar samples.

These results highlight the uncertainties in the chemical evolution of the NSD and the need for additional constraints beyond stellar abundances alone. In this context, measurements of the chemical composition of the interstellar medium, particularly in molecular clouds, provide a complementary probe of the ongoing enrichment processes in the Galactic centre. In particular, isotopic ratios, such as the $^{12}C/^{13}C$ studied in this work, are powerful diagnostics of nucleosynthetic enrichment and gas processing, as they trace the relative contributions of massive stars and intermediate-mass stars over time. Constraining these isotopic ratios in molecular clouds therefore provides important independent constraints on the star formation history, gas inflow, and mixing processes that shape the chemical evolution of the NSD.

5. Conclusions

We investigated the $^{12}C/^{13}C$ isotopic ratio toward the CMZ molecular cloud G+0.693−0.027 using observations of HC_3N, HC_5N, and their ^{13}C isotopologues. Our main findings are summarized as follows:

1. Using several ^{13}C isotopologues of HC_3N and HC_5N, we derived the $^{12}C/^{13}C$ ratio in G+0.693. For HC_3N, the main C1 extended, warm, and more diffuse velocity component ($T_{\rm kin}$=140 K and $n_{\rm H_2}$=2×10^4 cm^{-3}) yields $^{12}C/^{13}C$=36.7±1.02 based on double-^{13}C isotopologues. Moreover, the compact, colder, and denser C2 component ($T_{\rm kin}$=30 K and $n_{\rm H_2}$=5×10^4 cm^{-3}) gives $^{12}C/^{13}C$=26±3. For HC_5N, the average ratio obtained for C1 is $^{12}C/^{13}C$=38.8±1.5. Ratios derived from the main HC_3N isotopolog are strongly affected by line optical depth effects. The most reliable value for C1 comes from double-^{13}C isotopologues of HC_3N, and from single isotopologues of HC_5N. The combined average ratio of 37.7 ± 1.0 for C1 indicates that the carbon isotopic ratio in the CMZ is likely higher than previously adopted.
2. We used astrochemical modeling with the most up-to-date chemical models including ^{13}C- and ^{15}N-isotopologues, which suggests that the observed ratios correspond to a low to intermediate isotopic fractionation degree and are consistent with early chemical times ($\lesssim 3\times10^4$ yr) after the shock event affecting G+0.693. This provides a constraint on the initial $^{12}C/^{13}C$ ratio of the parent material of the CMZ clouds of ∼48.
3. The $^{12}C/^{13}C$ ratio derived in this work (∼37, increasing up to ∼48 when correcting for fractionation effects) lies at the upper end of the values reported for the CMZ and is consistent with measurements obtained using optically thin tracers and double-isotopolog methods. When compared with the Galactic gradient of the $^{12}C/^{13}C$ ratio, these values correspond to those typically found at galactocentric distances of ∼3–5 kpc, suggesting the presence of less chemically processed gas in the central region. Moreover, the derived ratios are comparable to those observed in the nuclear regions of nearby starburst and spiral galaxies, indicating that similar gas inflow and chemical enrichment processes may operate in galactic centers.

4. The high $^{12}C/^{13}C$ ratios derived in this work support a scenario in which the CMZ is replenished by less chemically processed gas, originating from larger galactocentric distances, or from the Galactic halo, with a possible contribution from the merging of external dwarf galaxies. From the perspective of stellar nucleosynthesis and chemical evolution models, such elevated ratios are consistent with the presence of recently accreted material that has experienced limited ^{13}C enrichment from long-lived AGB stars. Our results therefore provide independent constraints on the chemical evolution of the NSD, supporting scenarios in which sustained or episodic gas inflow from the inner Galactic disk fuels star formation and shapes the isotopic composition of the CMZ.

This study emphasizes the importance of combining different species, multiple isotopologues (including double ones), and astrochemical modeling to accurately derive and interpret isotopic ratios and, as a consequence, the chemical evolution of elements in chemically rich environments such as the CMZ. Such isotopic diagnostics are also becoming powerful tools in extragalactic studies, where measurements of molecular isotopic ratios in starburst galaxies can constrain the stellar initial mass function and the star formation history of distant systems (e.g., Zhang et al. 2018).

Acknowledgements. We thank the referee for the valuable comments and suggestions that improved the quality of the paper. We are very grateful to the Yebes 40m and IRAM 30m telescope staff for their precious help during the different observing runs. The 40m radio telescope at Yebes Observatory is operated by the Spanish Geographic Institute (IGN; Ministerio de Transportes, Movilidad y Agenda Urbana). IRAM is supported by INSU/CNRS (France), MPG (Germany) and IGN (Spain). The project that gave rise to these results received the support of a fellowship from the "la Caixa" Foundation (ID 100010434). The fellowship code is LCF/BQ/PR25/12110012. L.C, I.J.-S., V.M.R., and M.S.-N acknowledge support from the grant PID2022-136814NB-I00 funded by the Spanish Ministry of Science, Innovation and Universities/State Agency of Research MICIU/AEI/10.13039/501100011033 and by ERDF, UE. O.S. acknowledges the financial support of the Max Planck Society. I.J.-S. also acknowledges support by ERC grant OPENS, GA No. 101125858, funded by the European Union. Moreover, I.J.-S, L.C. and S.Z. acknowledge support from CSIC through ILINK project SENTINEL (ILINK23017) and Bilateral project SOULMATE (BIJSP25017). V.M.R. also acknowledges the grant CNS2023-144464 funded by MICIU/AEI/10.13039/501100011033 and by "European Union NextGenerationEU/PRTR". M.S.-N. also acknowledges funding from the Alexander von Humboldt foundation under a Humboldt Research Fellowship. We thank Dr. Donatella Romano and Prof. Serena Viti for fruitful discussions that helped to improve the interpretation of our results.

References

Aalto, S., Black, J. H., Booth, R. S., & Johansson, L. E. B. 1991a, A&A, 247, 291
Aalto, S., Black, J. H., Johansson, L. E. B., & Booth, R. S. 1991b, A&A, 249, 323
Aalto, S., Booth, R. S., Black, J. H., & Johansson, L. E. B. 1995, A&A, 300, 369
Aladro, R., Martín, S., Riquelme, D., et al. 2015, A&A, 579, A101
Aladro, R., Viti, S., Bayet, E., et al. 2013, A&A, 549, A39
Alexander, A. J., Kroto, H. W., & Walton, D. R. M. 1976, Journal of Molecular Spectroscopy, 62, 175
Araki, M., Sanz-Novo, M., Endres, C. P., et al. 2026, Nature Astronomy [arXiv:2511.23299]
Arcones, A. & Thielemann, F.-K. 2023, A&A Rev., 31, 1
Armijos-Abendaño, J., Banda-Barragán, W. E., Martín-Pintado, J., et al. 2020, MNRAS, 499, 4918
Battersby, C., Walker, D. L., Barnes, A., et al. 2025, ApJ, 984, 156
Belloche, A., Müller, H. S. P., Garrod, R. T., & Menten, K. M. 2016, A&A, 587, A91
Belloche, A., Müller, H. S. P., Menten, K. M., Schilke, P., & Comito, C. 2013, A&A, 559, A47
Berni, L., Palla, M., Magrini, L., & Spina, L. 2026, A&A, 707, A242
Bish, H. V., Werk, J. K., Prochaska, J. X., et al. 2019, ApJ, 882, 76
Bizzocchi, L., Degli Esposti, C., & Botschwina, P. 2004, Journal of Molecular Spectroscopy, 225, 145
Böhm, L. M., Jacob, A. M., Wyrowski, F., et al. 2026, A&A, 705, A80
Boogert, A. C. A., Ehrenfreund, P., Gerakines, P. A., et al. 2000, A&A, 353, 349
Boreiko, R. T. & Betz, A. L. 1991, ApJ, 380, L27
Botelho, R. B., Milone, A. d. C., Meléndez, J., et al. 2020, MNRAS, 499, 2196
Brünken, S., Belloche, A., Martín, S., Verheyen, L., & Menten, K. M. 2010, A&A, 516, A109
Burbidge, E. M., Burbidge, G. R., Fowler, W. A., & Hoyle, F. 1957, Reviews of Modern Physics, 29, 547
Butterworth, J., Viti, S., Van der Werf, P. P., et al. 2024, A&A, 686, A31
Caselli, P. & Ceccarelli, C. 2012, A&A Rev., 20, 56
Chabrier, G. 2003, ApJ, 586, L133
Chen, W., Bocquet, R., Wlodarczak, G., & Boucher, D. 1991, International Journal of Infrared and Millimeter Waves, 12, 987
Chen, Z., Do, T., Ghez, A. M., et al. 2023, ApJ, 944, 79
Chiappini, C., Ekström, S., Meynet, G., et al. 2008, A&A, 479, L9
Colzi, L., Fontani, F., Rivilla, V. M., et al. 2018, MNRAS, 478, 3693
Colzi, L., Martín-Pintado, J., Rivilla, V. M., et al. 2022a, ApJ, 926, L22
Colzi, L., Martín-Pintado, J., Zeng, S., et al. 2024, A&A, 690, A121
Colzi, L., Romano, D., Fontani, F., et al. 2022b, A&A, 667, A151
Colzi, L., Sipilä, O., Roueff, E., Caselli, P., & Fontani, F. 2020, A&A, 640, A51
Creswell, R. A., Winnewisser, G., & Gerry, M. C. L. 1977, Journal of Molecular Spectroscopy, 65, 420
Danielson, A. L. R., Swinbank, A. M., Smail, I., et al. 2013, MNRAS, 436, 2793
De Marchi, G., Habel, N., Meixner, M., et al. 2025, ApJ, 992, 203
de Zafra, R. L. 1971, ApJ, 170, 165
DeLeon, R. L. & Muenter, J. S. 1985, J. Chem. Phys., 82, 1702
Do, T., David Martinez, G., Kerzendorf, W., et al. 2020, ApJ, 901, L28
Dutkowska, K. M., Vermariën, G., Viti, S., et al. 2025, A&A, 703, A46
Encrenaz, P. J., Stark, A. A., Combes, F., & Wilson, R. W. 1979, A&A, 78, L1
Endres, C. P., Schlemmer, S., Schilke, P., Stutzki, J., & Müller, H. S. P. 2016, Journal of Molecular Spectroscopy, 327, 95
Feldmeier-Krause, A., Kerzendorf, W., Do, T., et al. 2020, MNRAS, 494, 396
Fomalont, E. B. & Weliachew, L. 1973, ApJ, 181, 781
Friske, J. K. S. & Schönrich, R. 2025, A&A, 701, A140
Gardner, F. F. & Whiteoak, J. B. 1979, MNRAS, 188, 331
Gardner, F. F. & Whiteoak, J. B. 1982, MNRAS, 199, 23P
Gerhard, O. 2011, Memorie della Societa Astronomica Italiana Supplementi, 18, 185
Giesen, T. F., Harding, M. E., Gauss, J., Grabow, J.-U., & Müller, H. S. P. 2020a, Journal of Molecular Spectroscopy, 371, 111303
Giesen, T. F., Mookerjea, B., Fuchs, G. W., et al. 2020b, A&A, 633, A120
Ginsburg, A., Bally, J., Barnes, A., et al. 2018, ApJ, 853, 171
Goldsmith, P. F. & Langer, W. D. 1999, ApJ, 517, 209
Goldsmith, P. F. & Linke, R. A. 1981, ApJ, 245, 482
Grieco, V., Matteucci, F., Ryde, N., Schultheis, M., & Uttenthaler, S. 2015, MNRAS, 450, 2094
Guesten, R., Henkel, C., & Batrla, W. 1985, A&A, 149, 195
Hachisuka, K., Choi, Y. K., Reid, M. J., et al. 2015, ApJ, 800, 2
Halfen, D. T., Woolf, N. J., & Ziurys, L. M. 2017, ApJ, 845, 158
Helmi, A., Babusiaux, C., Koppelman, H. H., et al. 2018, Nature, 563, 85
Henkel, C., Asiri, H., Ao, Y., et al. 2014, A&A, 565, A3
Henkel, C., Guesten, R., & Gardner, F. F. 1985, A&A, 143, 148
Henkel, C., Mauersberger, R., Wiklind, T., et al. 1993, A&A, 268, L17
Henkel, C., Walmsley, C. M., & Wilson, T. L. 1980, A&A, 82, 41
Henkel, C., Wilson, T. L., & Bieging, J. 1982, A&A, 109, 344
Henkel, C., Wilson, T. L., Walmsley, C. M., & Pauls, T. 1983, A&A, 127, 388
Henley, D. B., Shelton, R. L., Kwak, K., Joung, M. R., & Mac Low, M.-M. 2010, ApJ, 723, 935
Henshaw, J. D., Barnes, A. T., Battersby, C., et al. 2023, in Astronomical Society of the Pacific Conference Series, Vol. 534, Protostars and Planets VII, ed. S. Inutsuka, Y. Aikawa, T. Muto, K. Tomida, & M. Tamura, 83
Herbst, E. & van Dishoeck, E. F. 2009, ARA&A, 47, 427
Humire, P. K., Thiel, V., Henkel, C., et al. 2020, A&A, 642, A222
Ibata, R. A., Gilmore, G., & Irwin, M. J. 1994, Nature, 370, 194
Jacob, A. M., Menten, K. M., Wiesemeyer, H., et al. 2020, A&A, 640, A125
Jiang, X., Wang, J., & Gu, Q. 2011, MNRAS, 418, 1753
Jiménez-Serra, I., Martín-Pintado, J., Rivilla, V. M., et al. 2020, Astrobiology, 20, 1048
Jiménez-Serra, I., Rodríguez-Almeida, L. F., Martín-Pintado, J., et al. 2022, A&A, 663, A181
Jiménez-Serra, I., Viti, S., Quénard, D., & Holdship, J. 2018, ApJ, 862, 128
Johansson, L. E. B., Olofsson, H., Hjalmarson, A., Gredel, R., & Black, J. H. 1994, A&A, 291, 89
Jones, P. A., Burton, M. G., Cunningham, M. R., et al. 2012, MNRAS, 419, 2961
Karakas, A. I. & Lattanzio, J. C. 2014, PASA, 31, e030
Keene, J., Schilke, P., Kooi, J., et al. 1998, ApJ, 494, L107
Kikumoto, T., Taniguchi, Y., Nakai, N., et al. 1998, PASJ, 50, 309
Kobayashi, C., Karakas, A. I., & Lugaro, M. 2020, ApJ, 900, 179

Kovtyukh, V., Lemasle, B., Bono, G., et al. 2022, MNRAS, 510, 1894
Kovtyukh, V. V., Andrievsky, S. M., Martin, R. P., et al. 2019, MNRAS, 489, 2254
Kroupa, P., Tout, C. A., & Gilmore, G. 1993, MNRAS, 262, 545
Kruegel, E., Chini, R., & Steppe, H. 1990, A&A, 229, 17
Langer, W. D. & Penzias, A. A. 1990, ApJ, 357, 477
Li, F., Zhang, Z.-Y., Wang, J., et al. 2022, ApJ, 933, 139
Li, J., Wang, J., Qiao, H., et al. 2020, MNRAS, 492, 556
Loiseau, N., Nakai, N., Sofue, Y., et al. 1990, A&A, 228, 331
Loison, J.-C., Wakelam, V., Gratier, P., & Hickson, K. M. 2020, MNRAS, 498, 4663
Luo, G., Colzi, L., Liu, T., et al. 2024, A&A, 690, A372
Maiolino, R. & Mannucci, F. 2019, A&A Rev., 27, 3
Majewski, S. R., Skrutskie, M. F., Weinberg, M. D., & Ostheimer, J. C. 2003, ApJ, 599, 1082
Mallinson, P. D. & de Zafra, R. L. 1978, Molecular Physics, 36, 827
Margulès, L., Belloche, A., Müller, H. S. P., et al. 2016, A&A, 590, A93
Martín, S., Aladro, R., Martín-Pintado, J., & Mauersberger, R. 2010, A&A, 522, A62
Martín, S., Mangum, J. G., Harada, N., et al. 2021, A&A, 656, A46
Martín, S., Martín-Pintado, J., Blanco-Sánchez, C., et al. 2019a, A&A, 631, A159
Martín, S., Martín-Pintado, J., Montero-Castaño, M., Ho, P. T. P., & Blundell, R. 2012, A&A, 539, A29
Martín, S., Muller, S., Henkel, C., et al. 2019b, A&A, 624, A125
Martín, S., Requena-Torres, M. A., Martín-Pintado, J., & Mauersberger, R. 2008, ApJ, 678, 245
Matsunaga, N., Taniguchi, D., Elgueta, S. S., et al. 2023, ApJ, 954, 198
Matteucci, F. 2021, A&A Rev., 29, 5
Mauersberger, R. & Henkel, C. 1993, Reviews in Modern Astronomy, 6, 69
Meier, D. S., Walter, F., Bolatto, A. D., et al. 2015, ApJ, 801, 63
Milam, S. N., Savage, C., Brewster, M. A., Ziurys, L. M., & Wyckoff, S. 2005, ApJ, 634, 1126
Molaro, P., Aguado, D. S., Caffau, E., et al. 2023, A&A, 679, A72
Müller, H. S. P., Belloche, A., Menten, K. M., Comito, C., & Schilke, P. 2008, Journal of Molecular Spectroscopy, 251, 319
Müller, H. S. P., Belloche, A., Xu, L.-H., et al. 2016, A&A, 587, A92
Müller, H. S. P., Schlöder, F., Stutzki, J., & Winnewisser, G. 2005, Journal of Molecular Structure, 742, 215
Müller, H. S. P., Thorwirth, S., Roth, D. A., & Winnewisser, G. 2001, A&A, 370, L49
Muller, S., Guélin, M., Dumke, M., Lucas, R., & Combes, F. 2006, A&A, 458, 417
Myeong, G. C., Evans, N. W., Belokurov, V., Sanders, J. L., & Koposov, S. E. 2018, ApJ, 863, L28
Najarro, F., Figer, D. F., Hillier, D. J., Geballe, T. R., & Kudritzki, R. P. 2009, ApJ, 691, 1816
Palla, M., Magrini, L., Spitoni, E., et al. 2024, A&A, 690, A334
Papadopoulos, P. P., Zhang, Z.-Y., Xilouris, E. M., et al. 2014, ApJ, 788, 153
Prantzos, N., Abia, C., Limongi, M., Chieffi, A., & Cristallo, S. 2018, MNRAS, 476, 3432
Prantzos, N., Aubert, O., & Audouze, J. 1996, A&A, 309, 760
Requena-Torres, M. A., Martín-Pintado, J., Rodríguez-Franco, A., et al. 2006, A&A, 455, 971
Riquelme, D., Amo-Baladrón, M. A., Martín-Pintado, J., et al. 2010, A&A, 523, A51
Ritchey, A. M., Federman, S. R., & Lambert, D. L. 2011, ApJ, 728, 36
Rivilla, V. M., García De La Concepción, J., Jiménez-Serra, I., et al. 2022, Frontiers in Astronomy and Space Sciences, 9, 829288
Rivilla, V. M., Jiménez-Serra, I., Martín-Pintado, J., et al. 2021, Proceedings of the National Academy of Sciences, 118 [https://www.pnas.org/content/118/22/e2101314118.full.pdf]
Rivilla, V. M., Martín-Pintado, J., Jiménez-Serra, I., et al. 2020, ApJ, 899, L28
Rivilla, V. M., Martín-Pintado, J., Jiménez-Serra, I., et al. 2019, MNRAS, 483, L114
Rivilla, V. M., Sanz-Novo, M., Jiménez-Serra, I., et al. 2023, ApJ, 953, L20
Rizzuti, F., Cescutti, G., Molaro, P., et al. 2025, A&A, 698, A118
Rodríguez-Almeida, L. F., Jiménez-Serra, I., Rivilla, V. M., et al. 2021a, ApJ, 912, L11
Rodríguez-Almeida, L. F., Rivilla, V. M., Jiménez-Serra, I., et al. 2021b, A&A, 654, L1
Rodríguez-Fernández, N. J., Martín-Pintado, J., Fuente, A., & Wilson, T. L. 2004, A&A, 427, 217
Romano, D. 2022, A&A Rev., 30, 7
Romano, D., Matteucci, F., Zhang, Z.-Y., Ivison, R. J., & Ventura, P. 2019, MNRAS, 490, 2838
Romano, D., Matteucci, F., Zhang, Z. Y., Papadopoulos, P. P., & Ivison, R. J. 2017, MNRAS, 470, 401
Roueff, E., Loison, J. C., & Hickson, K. M. 2015, A&A, 576, A99
Ruiz-Lara, T., Mirabal, D., Gallart, C., et al. 2026, A&A, 705, A92
Ryde, N. & Schultheis, M. 2015, A&A, 573, A14
Sage, L. J. & Isbell, D. W. 1991, A&A, 247, 320
San Andrés, D., Rivilla, V. M., Colzi, L., et al. 2024, ApJ, 967, 39
Sanz, M. E., McCarthy, M. C., & Thaddeus, P. 2005, J. Chem. Phys., 122, 194319
Sanz-Novo, M., Rivilla, V. M., Endres, C. P., et al. 2025, ApJ, 980, L37
Sanz-Novo, M., Rivilla, V. M., Jiménez-Serra, I., et al. 2023, ApJ, 954, 3
Sanz-Novo, M., Rivilla, V. M., Jiménez-Serra, I., et al. 2024, ApJ, 965, 149
Savage, C., Apponi, A. J., Ziurys, L. M., & Wyckoff, S. 2002, ApJ, 578, 211
Schmiedeke, A., Schilke, P., Möller, T., et al. 2016, A&A, 588, A143
Schultheis, M., Rich, R. M., Origlia, L., et al. 2019, A&A, 627, A152
Sipilä, O., Colzi, L., Roueff, E., et al. 2023, A&A, 678, A120
Sliwa, K., Wilson, C. D., Iono, D., Peck, A., & Matsushita, S. 2014, ApJ, 796, L15
Sliwa, K., Wilson, C. D., Krips, M., et al. 2013, ApJ, 777, 126
Solomon, P. M., Radford, S. J. E., & Downes, D. 1990, ApJ, 348, L53
Sormani, M. C. & Barnes, A. T. 2019, MNRAS, 484, 1213
Spilker, J. S., Marrone, D. P., Aguirre, J. E., et al. 2014, ApJ, 785, 149
Spitoni, E., Schultheis, M., Matteucci, F., et al. 2026, A&A, 707, A202
Stark, A. A. & Carlson, E. R. 1984, ApJ, 279, 122
Tang, X. D., Henkel, C., Menten, K. M., et al. 2019, A&A, 629, A6
Tautvaišienė, G., Drazdauskas, A., Bragaglia, A., Randich, S., & Ženovienė, R. 2016, A&A, 595, A16
Tercero, B., Marcelino, N., Roueff, E., et al. 2024, A&A, 682, L12
Thorsbro, B., Ryde, N., Rich, R. M., et al. 2020, ApJ, 894, 26
Thorwirth, S., Mueller, H. S. P., & Winnewisser, G. 2001, Physical Chemistry Chemical Physics (Incorporating Faraday Transactions), 3, 1236
Thorwirth, S., Müller, H. S. P., & Winnewisser, G. 2000, Journal of Molecular Spectroscopy, 204, 133
Tress, R. G., Sormani, M. C., Glover, S. C. O., et al. 2020, MNRAS, 499, 4455
Turner, B. E. 1991, ApJS, 76, 617
Viti, S., Fontani, F., & Jiménez-Serra, I. 2020, MNRAS, 497, 4333
Wallström, S. H. J., Muller, S., & Guélin, M. 2016, A&A, 595, A96
Wang, M., Chin, Y.-N., Henkel, C., Whiteoak, J. B., & Cunningham, M. 2009, ApJ, 690, 580
Wannier, P. G. & Linke, R. A. 1978, ApJ, 226, 817
Whiteoak, J. B., Dahlem, M., Wielebinski, R., & Harnett, J. I. 1990, A&A, 231, 25
Wiklind, T. & Henkel, C. 1990, A&A, 227, 394
Wiklind, T. & Henkel, C. 1992, A&A, 257, 437
Wilson, T. L. & Matteucci, F. 1992, A&A Rev., 4, 1
Wilson, T. L. & Rood, R. 1994, ARA&A, 32, 191
Winnewisser, G., Winnewisser, M., & Christiansen, J. J. 1982, A&A, 109, 141
Woosley, S. E., Heger, A., & Weaver, T. A. 2002, Reviews of Modern Physics, 74, 1015
Wouterloot, J. G. A. & Brand, J. 1996, A&AS, 119, 439
Yamada, K. M. T., Moravec, A., & Winnewisser, G. 1995, Zeitschrift Naturforschung Teil A, 50, 1179
Yan, Y. T., Henkel, C., Kobayashi, C., et al. 2023, A&A, 670, A98
Yan, Y. T., Zhang, J. S., Henkel, C., et al. 2019, ApJ, 877, 154
Young, J. S. & Sanders, D. B. 1986, ApJ, 302, 680
Zeng, S., Jiménez-Serra, I., Rivilla, V. M., et al. 2018, MNRAS, 478, 2962
Zeng, S., Rivilla, V. M., Jiménez-Serra, I., et al. 2023, MNRAS, 523, 1448
Zeng, S., Zhang, Q., Jiménez-Serra, I., et al. 2020, MNRAS, 497, 4896
Zhang, Z.-Y., Romano, D., Ivison, R. J., Papadopoulos, P. P., & Matteucci, F. 2018, Nature, 558, 260
Zheng, S., Li, J., Wang, J., et al. 2024, ApJ, 961, 58

Appendix A: Supplementary observed spectra and model fits

In this appendix we show the observed spectra and the fit to those molecules studied in this work but not shown in the main text: $HC^{13}CCN$, $HCC^{13}CN$, $H^{13}C^{13}CCN$, $H^{13}CC^{13}CN$, $H^{13}CC_4N$, $HC^{13}CC_3N$, $HC_3^{13}CCN$, and $HC_2^{13}CC_2N$ (Figs. A.1–A.6).

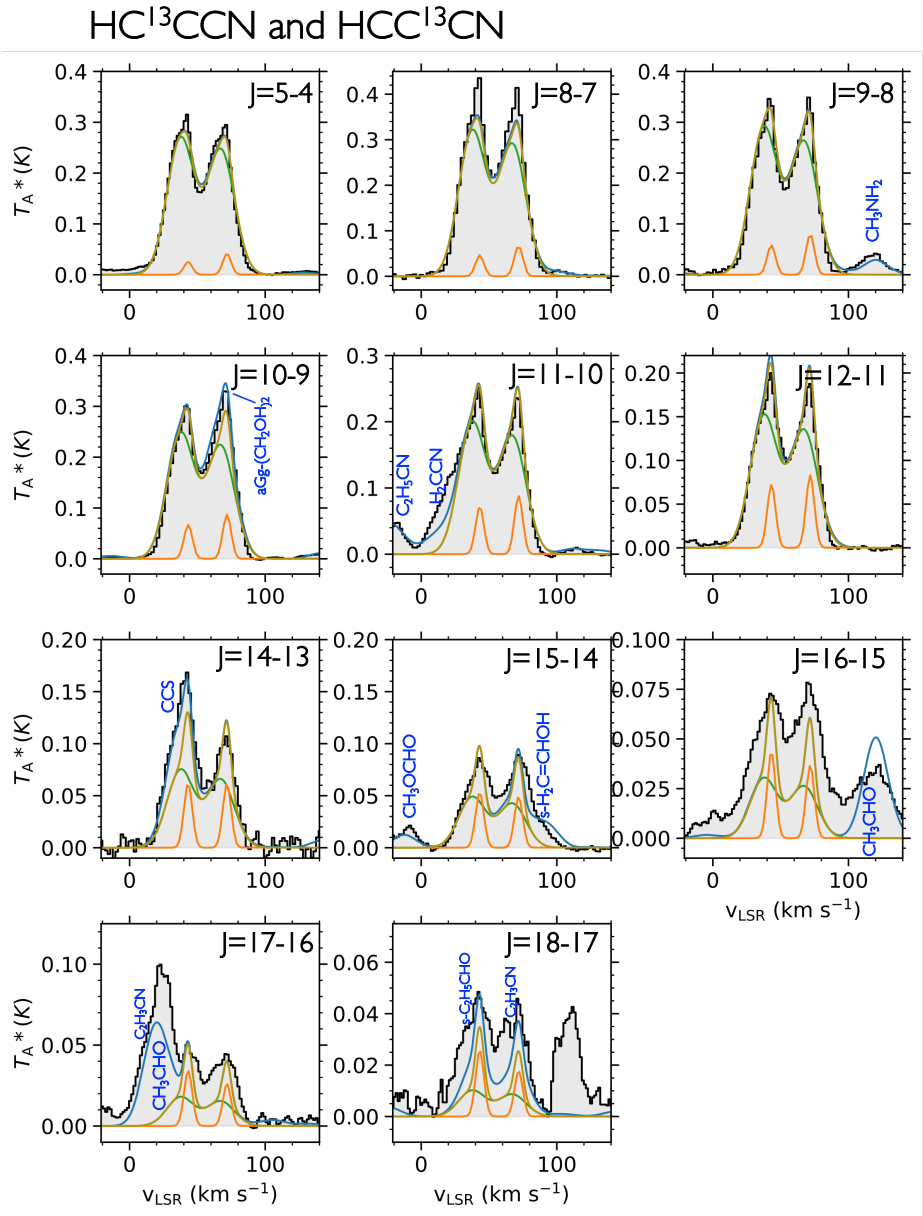

Fig. A.1: Same as Fig. 1 but for $HC^{13}CCN$ and $HCC^{13}CN$.

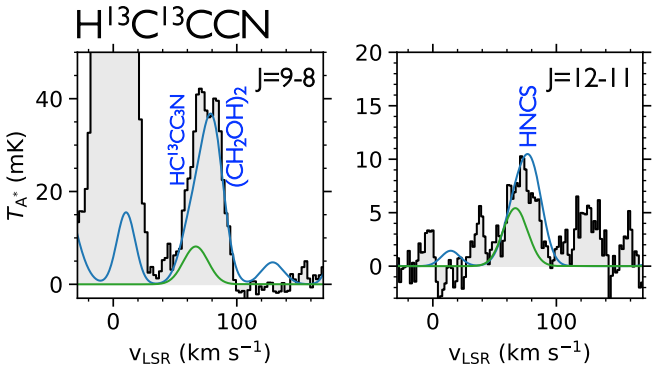

Fig. A.2: Same as Fig. 2 but for $H^{13}C^{13}CCN$. As explained in Sect. 3.1, this molecules is tentatively detected and we consider its column density as an upper limit.

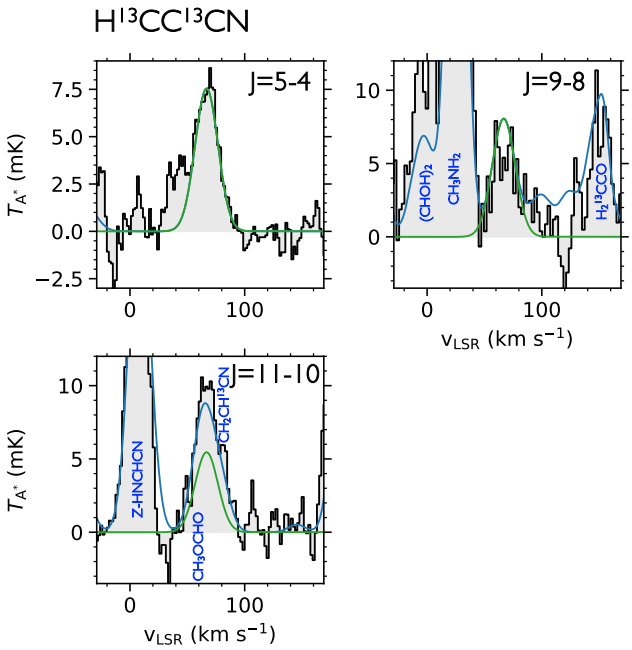

Fig. A.3: Same as Fig. 2 but for $H^{13}CC^{13}CN$.

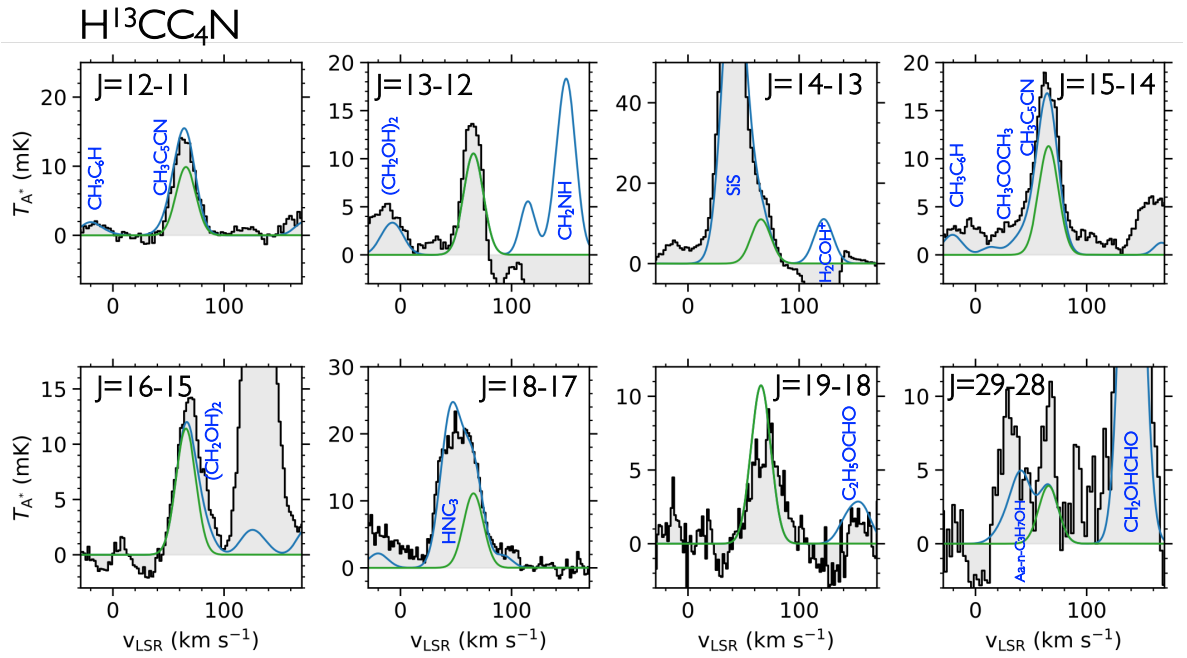

Fig. A.4: Same as Fig. 2 but for $H^{13}CC_4N$.

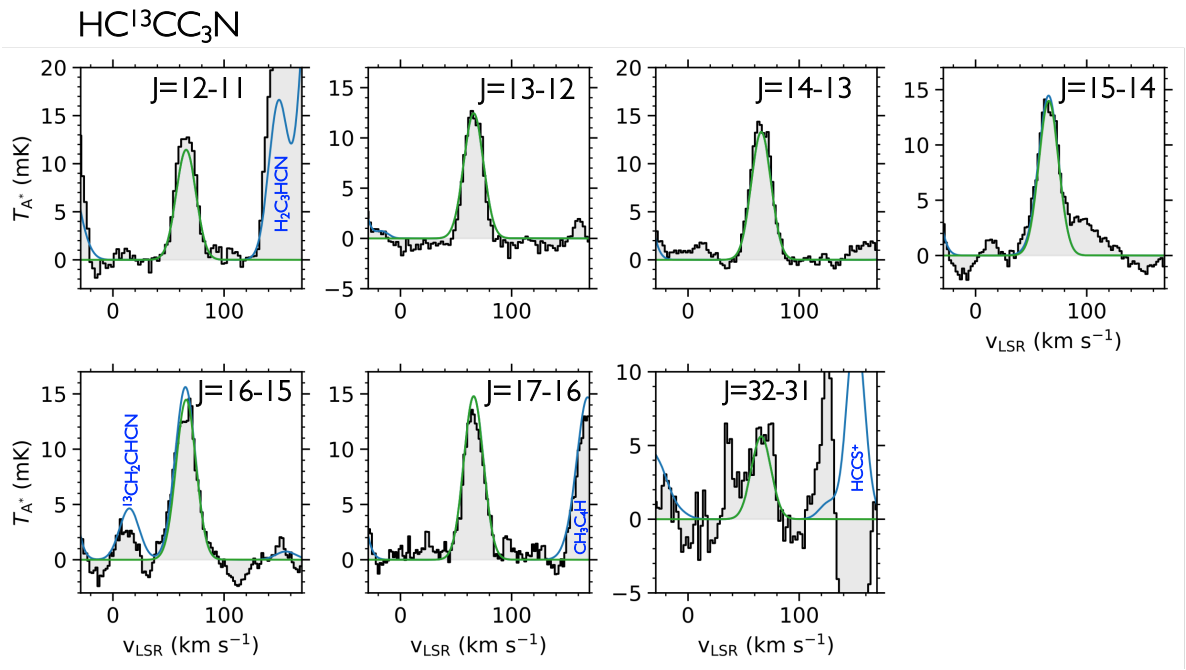

Fig. A.5: Same as Fig. 2 but for $HC^{13}CC_3N$.

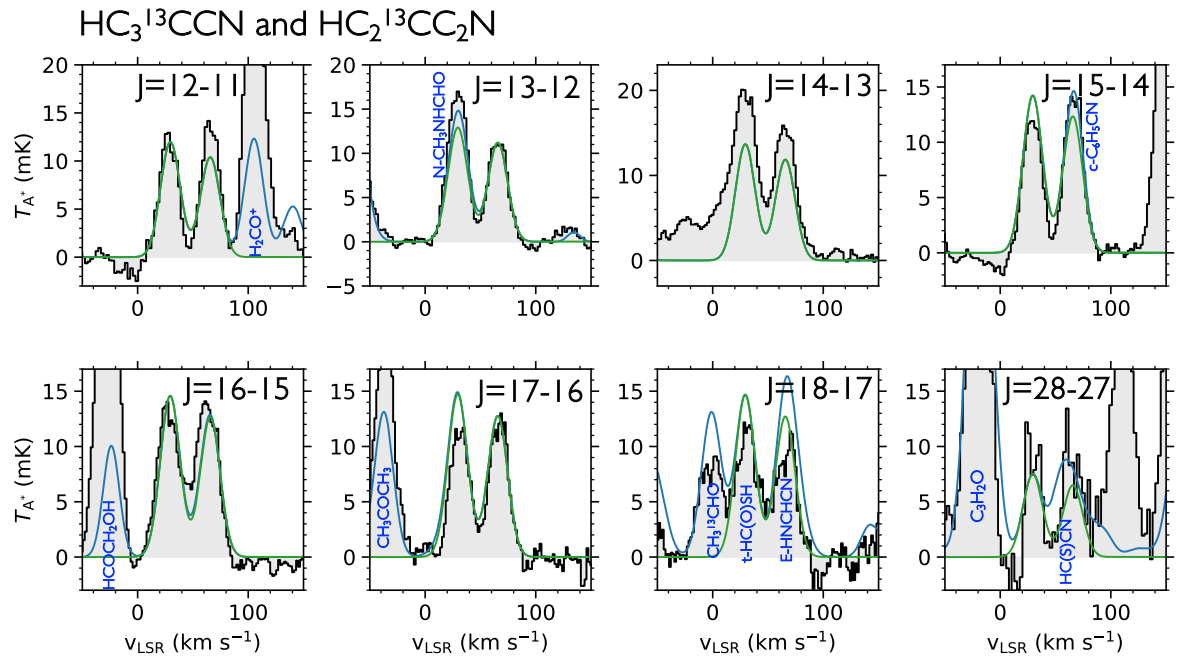

Fig. A.6: Same as Fig. 2 but for $HC_3^{13}CCN$ and $HC_2^{13}CC_2N$.

Appendix B: Observed transitions of HC_5N in G+0.693

In this appendix, we present the transitions of HC_5N detected toward G+0.693 and analyzed in Sect. 3.1. The transitions are divided into two groups: the low-J lines, spanning J = 12–11 to J = 32–31 (Fig. B.1), and the high-J lines, ranging from J = 33–32 to J = 43–42 (Fig. B.2).

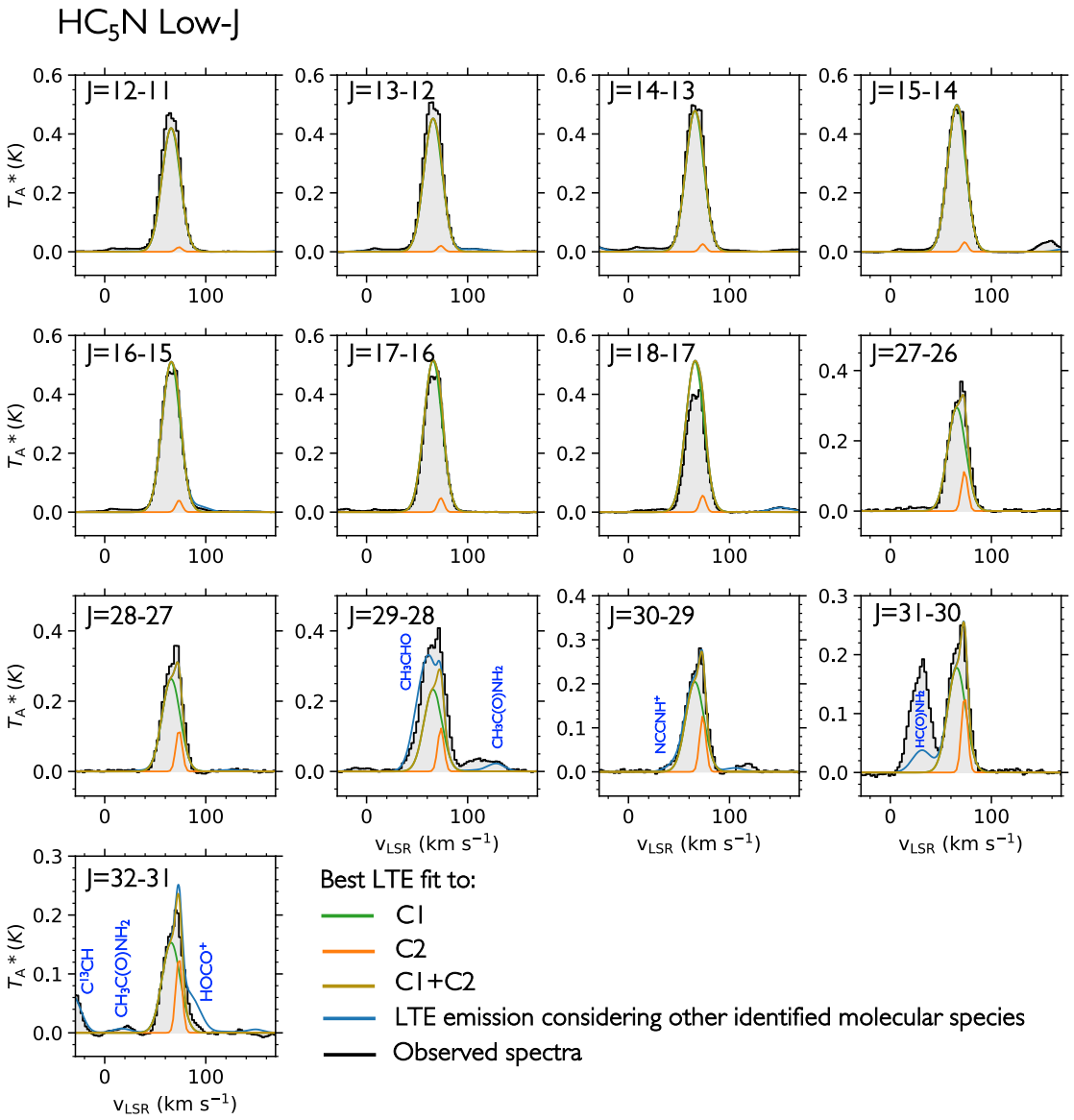

Fig. B.1: HC_5N observed low-J transitions used for the LTE analysis (black histogram). For each panel, the corresponding transition is indicated in the upper right corner and the telescope information is given if the same transition is observed with more than one instrument. The green and orange solid lines are the best LTE fit to the C1 and C2 components, respectively. The dark gold line is the sum of the two components. The blue line indicates the total modeled line emission, including the contribution of all molecular species previously identified in the survey (e.g., Zeng et al. 2018; Rodríguez-Almeida et al. 2021b,a; Rivilla et al. 2021; Sanz-Novo et al. 2023).

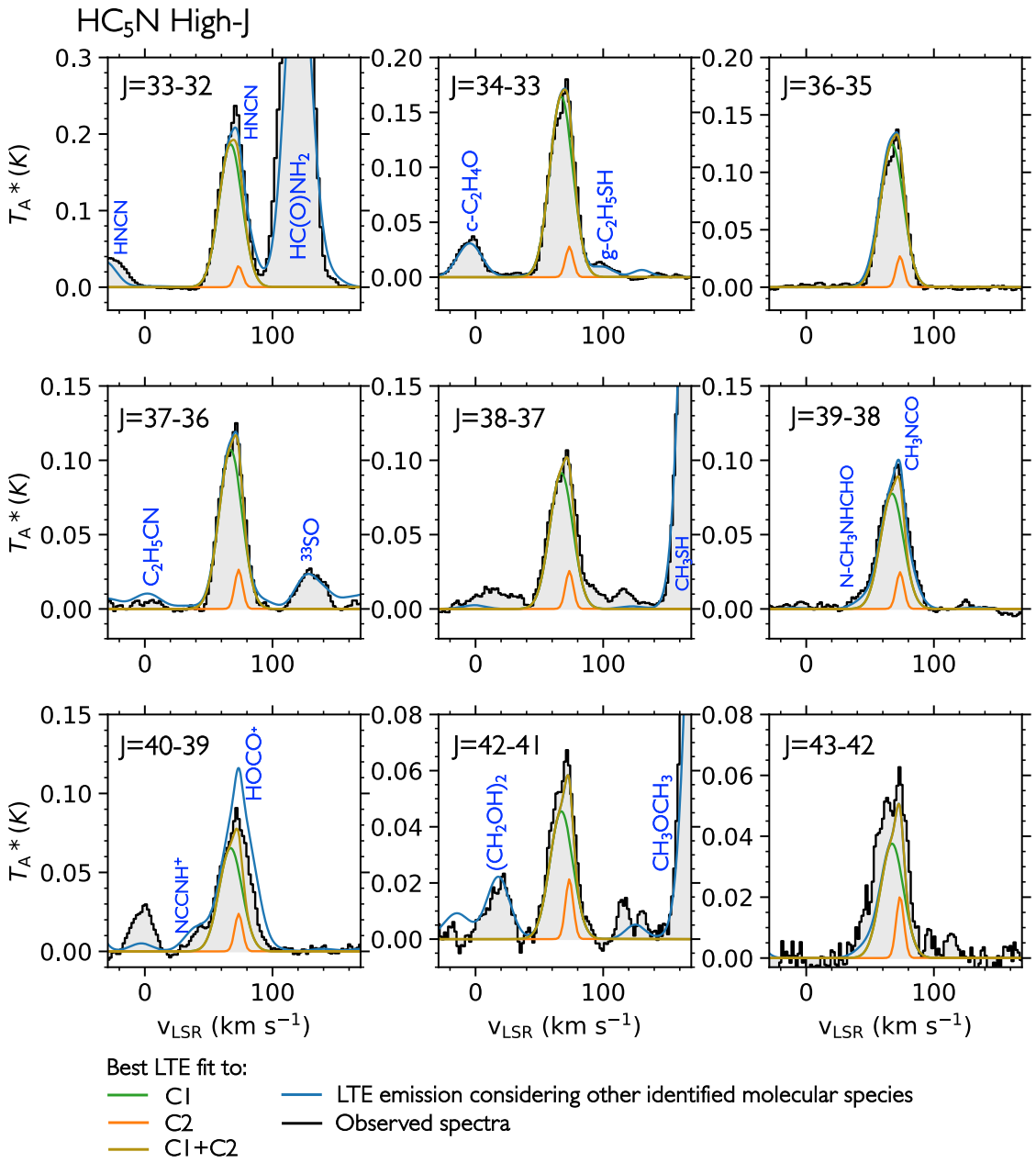

Fig. B.2: Same as Fig. B.1 but for high-J transitions.

Appendix C: LTE fit results

In this Appendix we present the results of the LTE fitting procedure for the molecules studied in this work.

Table C.1: Results from the LTE fitting procedure.

Molecule	Component	FWHM (km s^{-1})	v_{LSR} (km s^{-1})	T_{ex} (K)	N ($\times10^{14}$ cm^{-2})
			HC_3N		
HC_3N[a]	C1	23.52±0.17	67.79±0.09	16.53±0.15	6.54±0.07
	C2	7.2±0.6	73.5[b]	14.5±1.7	9±3
$H^{13}CCCN$	C1	23.5[b]	66.92±0.12	11.4±0.1	0.380±0.004
	C2	7.2	72.53±0.16	14.5±0.6	0.39±0.04
$HC^{13}CCN$	C1	23.5	67.32±0.17	11.03±0.16	0.372±0.007
	C2	7.2	71.9±0.2	14.5±0.9	0.41±0.05
$HCC^{13}CN$	C1	23.5	66.63±0.15	11.25±0.15	0.407±0.006
	C2	7.2	72.2	17.2±1.3	0.27±0.04
$H^{13}C^{13}CCN$	C1	23.5	66.8	13.8	<0.01[c]
	C2	7.2	72.1	14.5	<0.018[d]
				17.2	<0.022[d]
$H^{13}CC^{13}CN$	C1	23.5	66.8±1.3	10.9±1.4	0.0117±0.0014
	C2	7.2	72.1	14.5	<0.013[e]
				17.2	<0.015[e]
$HC^{13}C^{13}CN$	C1	23.5	66.8	17±3	0.0095±0.0010
	C2	7.2	72.1	14.5	<0.029[f]
				17.2	<0.032[f]
			HC_5N		
HC_5N low-J[g]	C1	21.0±0.2	65.70±0.14	19.0±0.2	1.247±0.018
	C2	7.2	73.5	36±9	1.7±0.3
HC_5N high-J	C1	21.0	67.2±0.2	22.9±0.5	1.12±0.07
	C2	7.2	73.5	36	0.34±0.05
$H^{13}CC_4N$	C1	21.0	65.7	16.2±1.6	0.0288±0.0013
	C2	7.2	73.5	36	<0.098[h]
$HC^{13}CC_3N$	C1	21.0	65.87±0.18	21.0±0.7	0.0355±0.0005
	C2	7.2	73.5	36	<0.098[i]
$HC_2^{13}CC_2N$	C1	21.0	65.7	19	0.0302±0.0010
	C2	7.2	73.5	36	<0.075[h]
$HC_3^{13}CCN$	C1	21.0	66.0±0.4	19	0.0347±0.0010
	C2	7.2	73.5	36	<0.124[i]
$HC_4^{13}CN$	C1	21.0	65.7	17.6 ±0.5	0.0324±0.0010
	C2	7.2	73.5	36	<0.060[h]

Notes. [(a)] Taken from Table 2 of Colzi et al. (2024). [(b)] Parameters without errors are fixed in the fitting procedure, as explained in Sect. 3.1 and in Colzi et al. (2024). [(c)] All the transitions are contaminated by other species. Upper limits calculated by hand simulating the maximum intensity that can reproduce the observed spectra (see Fig. A.2). [(d)] Upper limit calculated as explained in Sect. 3.1, taking into account the rms of 3 mK at 105 GHz. [(e)] Taking into account the rms of 0.5 mK at 44 GHz. [(f)] Taking into account the rms of 0.6 mK at 36 GHz. [(g)] Only the low-J transitions are used to calculate the isotopic ratios since the high-J transitions are not detected for the ^{13}C isotopologues. [(h)] Taking into account the rms of 0.7 mK at 34 GHz. [(i)] Taking into account the rms of 0.7 mK at 31 GHz.

Appendix D: Main chemical pathways leading to HC_3N and HC_5N

In this Appendix we present the main chemical pathways leading to the formation of HC_3N and HC_5N in the models presented in Sect. 3.2.

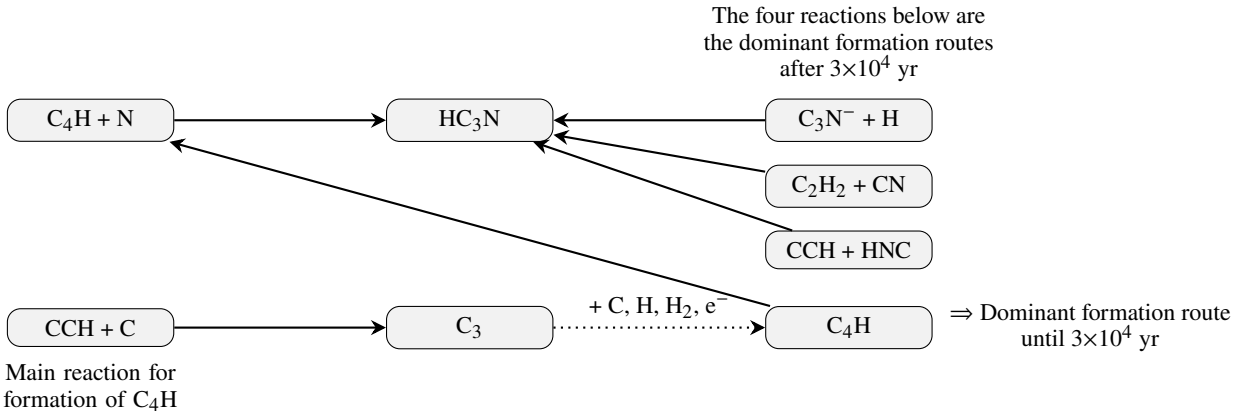

Fig. D.1: Schematic representation of the main chemical pathways leading to the formation of HC_3N. The dominant route proceeds via the neutral-neutral reaction C_4H + N, while additional neutral and ion–neutral reactions contribute at later times. The dotted arrows indicate that this part of the pathway comprises multiple reactions that are not shown explicitly.

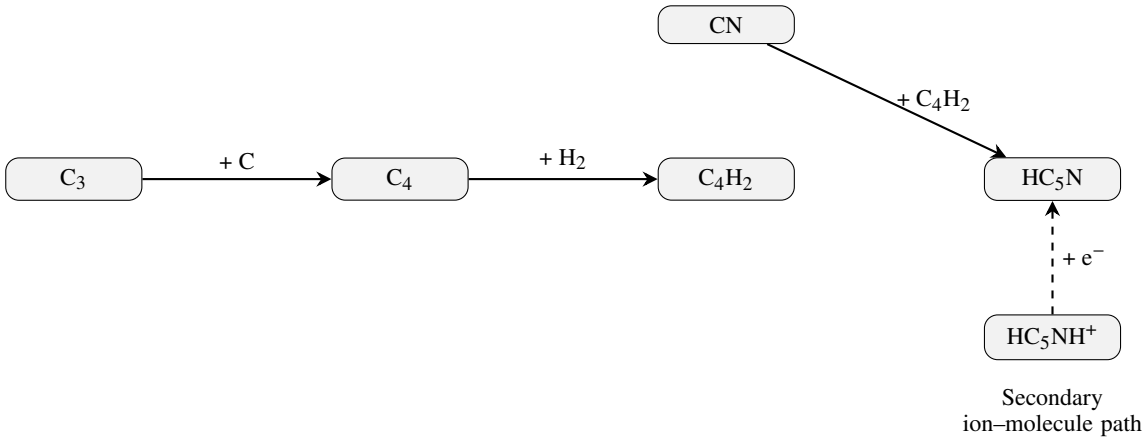

Fig. D.2: Simplified chemical network illustrating the main formation routes of HC_5N in the interstellar medium. C_3 contributes indirectly by forming longer carbon chains ($C_3 \rightarrow C_4 \rightarrow C_4H_2$), which then react with CN to produce HC_5N. The dashed arrow indicates an alternative ion–molecule pathway.